Delft University of Technology

Evaluating the Effect of Rock Typing for Carbonate Reservoirs in the Upper Kharaib Member, Rub Al Khali Basin on CO_2 Storage and Migration

Author:
Ghada Alshaikhmubarak (5860954)
Thesis Committee:
Sebastian Geiger(Thesis Supervisor - TU Delft)
Guillaume Rongier (TU Delft)
Alexandros Daniilidis (TU Delft)

March 10, 2025

Abstract

This research evaluates the effect of rock typing on CO_2 storage capacity and plume migration in the Upper Kharaib carbonate reservoir, located in the Rub Al Khali Basin. The open source COSTA model was used to apply two rock typing methods, the Winland R35 classification and the Flow Zone Indicator, and were compared to the general relationship of the base method to characterize the relationship between porosity and permeability. Rock typing methods demonstrated results that had high amount of CO_2 stored, high vertical upward plume migration towards the structural trap, and good pressure distribution due to its high permeability compared to the base method. The results showed that the Winland R35 classification method had the highest storage capacity of 136.7 $MtCO_2$ followed by the Flow Zone Indicator at 109.1 $MtCO_2$, and the base method at a maximum of only 54.9 $MtCO_2$. Furthermore, an uncertainty analysis on the porosity model generated multiple realizations. It showed low variability in the base method simulation results for the amount of CO_2 stored and higher variability in the results for rock-typing that introduces higher uncertainty. Rock-typing methods show a higher CO_2 storage potential but could be associated with higher uncertainty that requires careful consideration. This research provides findings on rock-typing methods CO_2 storage potential and the uncertainities associated for future carbon capture and storage (CCS) projects in carbonate reservoirs.

Acknowledgments

I would like to express my deepest appreciation to my thesis supervisor Sebastian Geiger, for his constant support and guidance throughout this project. I would like to extend my sincerest appreciation to the members of the thesis committee, Guillaume Rongier and Alexandros Daniilidis, for their invaluable feedback and support.

I am incredibly Thankful to Saudi Aramco for giving me this opportunity and sponsoring this Master's degree, and thankful to Brahim Hamouche for his support.

I am deeply grateful to my loved ones for their constant encouragement, unwavering support, and boundless care. Your presence in my life is a true blessing, and I am forever thankful for you.

Contents

List of Figures

List of Tables

1 Introduction

The world is currently facing a major challenge, climate change, as greenhouse gases (GHG) in the atmosphere are the main contributors to this, with carbon dioxide (CO_2) among them (Lindsey, 2024). Since the industrial revolution, CO_2 emissions have increased significantly, reaching 418 parts per million (ppm). This increase has occurred rapidly over the last 100 years, largely due to human activities related to the burning of fossil fuels (Lindsey, 2024). For years, the fossil fuel industry's had their own climate projections models that only recently received attention. An analysis of ExxonMobil internal company records between 1977 and 2003 showed that the company's scientists developed a range of global warming projections. Most of these projections match the observed warming trends, and are closely accurate to the independent academic and government models. These projections predicted the detection of human-induced warming, and provided estimates of the carbon budget increases to 2°. But these studies were downplayed in companies' public statements on climate science (Supran et al., 2023). Recent research has quantified the human costs associated with these environmental impacts, ranging from public statements that often downplayed these early warnings, the convergence of independent academic models and internal projections underscores the critical need to address climate change proactively (cite Supran et al., 2023).
As part of mitigation and efforts to reduce emissions, in 2015, the United Nations Framework Convention on Climate Change (UNFCC) established the Paris Agreement. This agreement urges participating countries to reduce their emissions in order to meet the 43% reduction goal of GHG in 2030 and the zero-emission goal of 2050. The purpose of the agreement is to limit the temperature increase to 1.5 °C instead of the currently expected increase of 2°C compared to the pre-industrial temperature level (unfccc.int, nd). One strategy to achieve these goals is carbon capture and storage (CCS).

1.1 Carbon capture and storage

Carbon capture and storage is a method that captures CO_2 from large sources such as power plants and industrial facilities before it is released into the atmosphere. After CO_2 is captured, it is transported through pipelines and then injected into a deep geological formation or depleted hydrocarbon fields. This approach helps to store large amounts of CO_2 securely for extended periods of time (National Grid Group, nd).
Today, this strategy is being considered in many countries as part of their efforts to reduce emissions and meet their commitments to the agreement. A great example for an implemented project is the Sleipner project in Norway, which has been storing CO_2 in a deep saline aquifer located in the North Sea since 1996. The project has stored around 15.5 million tons of CO_2 in 2015 since it began, demonstrating the effectiveness of CCS in reducing emissions (Furre et al., 2024). The Sleipner project targets the Utsira Sand Formation, but carbonates also hold great potential for CCS, as almost half of the current producing hydrocarbon fields are carbonates (Ahr, 2011). These fields are well studied and provide a lot of geological, petrophysical and production data that can be leveraged in assessing the potential of carbonate aquifers for CCS.
These data can help in the prediction of stored CO_2 volumes and its migration behavior in CCS. Specifically, petrophysical data, such as porosity and permeability, can influence CO_2 flow and storage. Therefore, understanding the relationship between them is crucial when assessing CCS potential reservoir. By applying different rock typing methods that give a variety of relationships between porosity and permeability, it improves understanding of quantifying predictive CO_2 stored and behavior, as well as quantifying and reducing the uncertainties in these predictions.

1.2 Reservoir rock typing

In general, a reservoir has differences in geological properties with variations in porosity and permeability that affect the flow behavior and storage capacity of the reservoir. To find the relationship between these properties, rock typing comes into place, as it is a method to characterize the reservoir by classifying rocks into different classes with similar behavior properties. It helps in identifying a relationship between porosity and permeability by analyzing the well log and core data to find trends in layers and samples that display the same porosity and permeability ranges (Tavakoli, 2018). There are many methods of rock typing, such as the Winland Classification and the Flow Zone Indicator, which will be discussed further in the next chapter (Skalinski and Kenter, 2015). Rock typing has been widely used in oil and gas reservoirs in order to link the petrophysics to sedimentology for reservoir characterization and management. As generally when rock typing is connected to facies, it helps in reducing the uncertainty in the static model. Therefore, it optimizes well placement and production plan as well as the enhanced recovery volumes.

1.3 Geological background

The Hajar supergroup is located in the United Arab Emirates and Oman. It is dominated by shallow marine to intertidal carbonate platform succession. During the Triassic, the Hajar supergroup was formed due to the opening of the southern Neotethys Ocean with distribution of rocks resulting from processes associated with the closure of the Neotethys ocean. It was developed during the Permian to lower Cretaceous on the Arabian continental passive margin. Part of this supergroup is the Thamama group where Upper Kharaib Member is deposited(Phillips et al., 2013). The Upper Kharaib is exposed in northern part of the United Arab Emirates as a series of anticline structures shown in Figure 1 that are part of the Thamama B group (Taher, 1997). It is late Barremian to early Aptian in age, where it was buried along the Oman margin during the Late Cretaceous and was deformed and exposed due to the uplift that occurred during the Miocene(van Buchem et al., 2002).

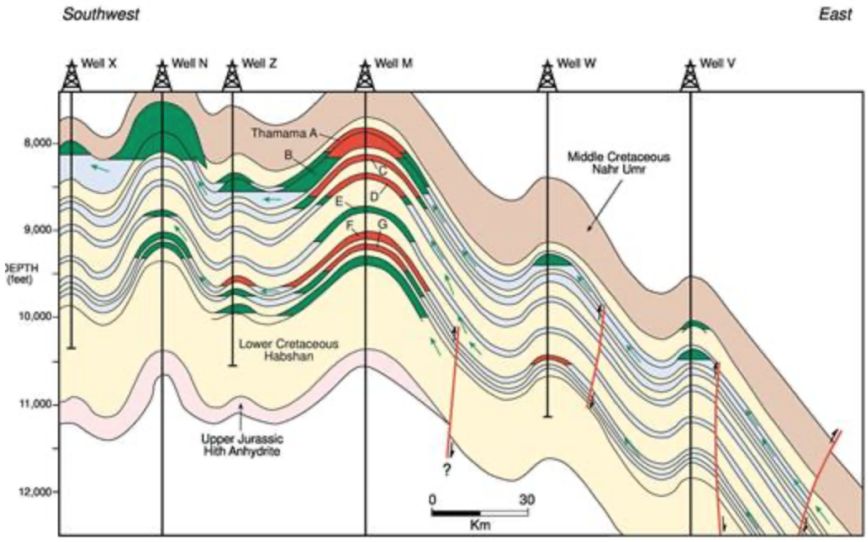

Figure 1: Structural cross-section SW-E of Upper Kharaib Member in the UAE in Thamama layer B (Taher, 1997).

The Upper Kharaib Member is mainly limestone with different textures and depositional features. Figure 2 shows the different depositional settings in the Upper Kharaib formation. Starting from the west, it has a flat ramp setting within the intrashelf basin and is characterized as shallow- water carbonates, with wackstone and packstone deposits in the inner ramp. In the inner to mid ramp, grainstone deposits can be found. And in the outer ramp it is mostly dominated by mudstone (van Buchem et al., 2002).

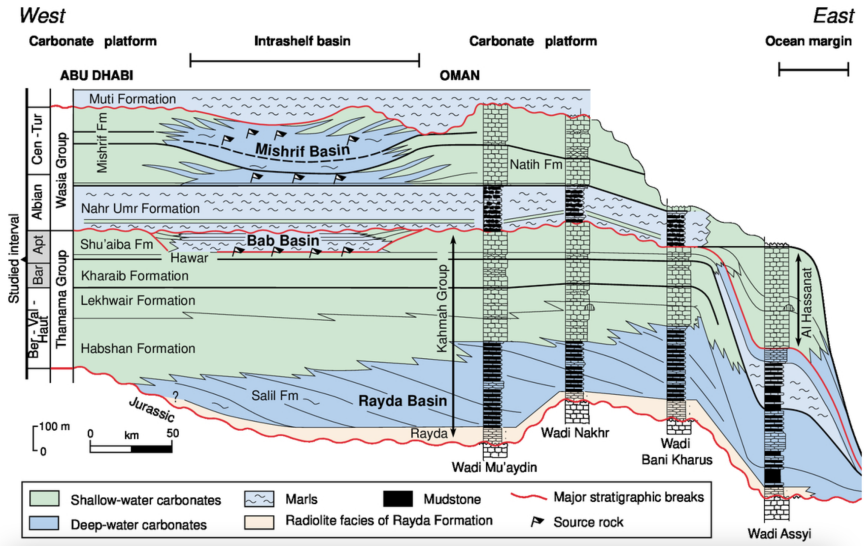

Figure 2: Schematic cross section of the regional stratigraphic between Oman and Abu Dhabi, in the lower and mid cretaceous (van Buchem et al., 2002).

1.4 Purpose of research

The aim of the research is to evaluate the effect of rock typing for carbonate reservoirs on CO_2 storage and plume migration. The research focuses on applying petrophysical characterization approaches and evaluating their impact on CO_2 storage and plume migration. The research highlights the uncertainties associated with the use of rock typing methods in heterogeneous reservoirs such as the Upper Kharaib member, as the choice of rock typing method can introduce uncertainty in predicting CO_2 storage and plume migration.

1.4.1 Research questions

The research focuses on the following questions:

- What is the effect of rock typing on CO_2 storage capacity?
- How does the CO_2 plume behavior differ in the rock typing methods?
- What are the uncertainties in rock typing methods in the static model and how is it related to uncertainty in predicting CO_2 storage?

1.4.2 Research workflow

The research starts by utilizing an open source model for the Upper Kharaib carbonate reservoir and retrieving the data into Petrel software developed by Schlumberger. In Chapter 2: Data and methodology presents the data set and data cleaning process, as it is the main input for the research. This is followed by a petrophysical analysis on the relationship between porosity and permeability, where three methods are applied, the general relationship method, and two rock typing methods. Subsequently, the static modeling workflow for porosity, rock type, and permeability is presented, showing that different rock types lead to different permeability values and distributions. Next, resampling is performed based on different well combinations to cross-validate. Chapter 2 continues to the dynamic modeling and simulation, where the reservoir grid is imported into a commercial reservoir simulator GEMS by CMG Ltd. The reservoir standard condition parameters, initial conditions, injection well placement, and boundary conditions are set for the simulator.
In Chapter 3, the results for the static modeling and uncertainties related to rock typing are discussed, along with the cross-validation results. In addition, showing the results for the simulation of the different models to evaluate the effect of rock types on CO_2 storage and plume migration to further assess the uncertainties associated with the rock typing methods. The chapter continues to address the study limitations and implications on the research. Finally, Chapter 4 concludes the findings and provides recommendations for future work.

2 Data and Methodology

This chapter focuses on existing data set, defining the porosity-permeability relationship and associated rock types. It also covers property modeling for porosity, rock types, and permeability. The chapter later continues with the methods used to set reservoir grid properties, relative permeability curves, initialization condition, well placement, and boundary condition.

2.1 Data set

The data set was retrieved from the COSTA model, an open source model developed by Jorge Costa Gomes. It has a synthetic reservoir based on real data that has been anonymised, scaled, and repositioned to represent the geometries and properties of carbonate reservoirs in the Middle East. The model is an analogue of the carbonate formation of the Upper Kharaib Member located in the Rub Al Khali region. The Upper Kharaib crosses many countries of the Arabian Gulf and is currently operating offshore and onshore for hydrocarbons (Figure 3). The model is 36,000 km^2 in area with 43 wells focusing on Layer B of the Upper Kharaib formation in the United Arab Emirates (U.A.E) and is heterogeneous in both upper and lower sections (Gomes, 2022).

The Winland classification, driven by capillary pressure, was used to generate different pore throat size distributions and identify rock types. The model also accounts for uncertainties related to the petrophysical and geomodeling approaches. The results of the model did show that the petrophysical characterization through rock typing did indeed have an impact on the reservoir volume and performance. It is considered a data source for carbonate reservoirs to explore the effect of rock typing on CO_2 storage and plume migration, which has not yet been studied (Gomes, 2022).

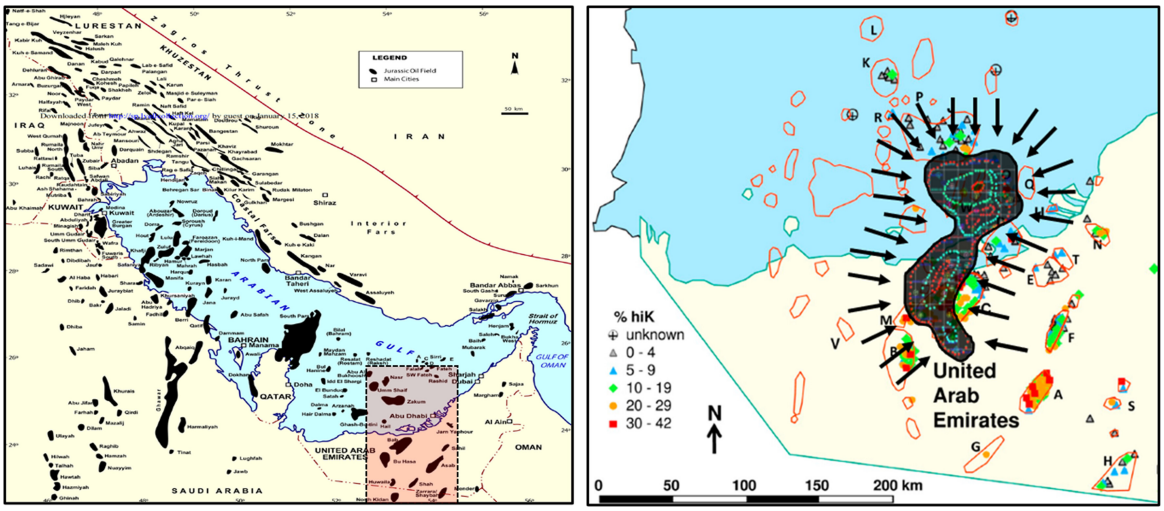

Figure 3: Left figure shows the geographic region of the middle east with the area of interest highlighted in red (Alsharhan, 2014). Right figure shows the major producing oil fields in the northeastern part of Rub Al Khali, in U.A.E (Ehrenberg et al., 2020). The center of the right figure highlighted in black illustrates the COSTA model theoretical structure in attempt to capture the carbonate formation from shelf-to-basin (Gomes, 2022).

2.1.1 Existing data

The retrieved data includes 43 wells that are scattered over an area of interest of 1.9 x 10^7 km^2 shown in Figure 4 with no faults or fractures. The available wells included 17 wells highlighted in red with open hole logs, core data, and well tops of the top and base of the reservoir. The open hole log data include gamma rays, neutron porosity, density, deep resistivity, and effective porosity along the reservoir depth interval. The same wells have core porosity and permeability from conventional core analysis with 0.5 ft over the entire reservoir interval; therefore, the core captures the reservoir permeability behavior against porosity.

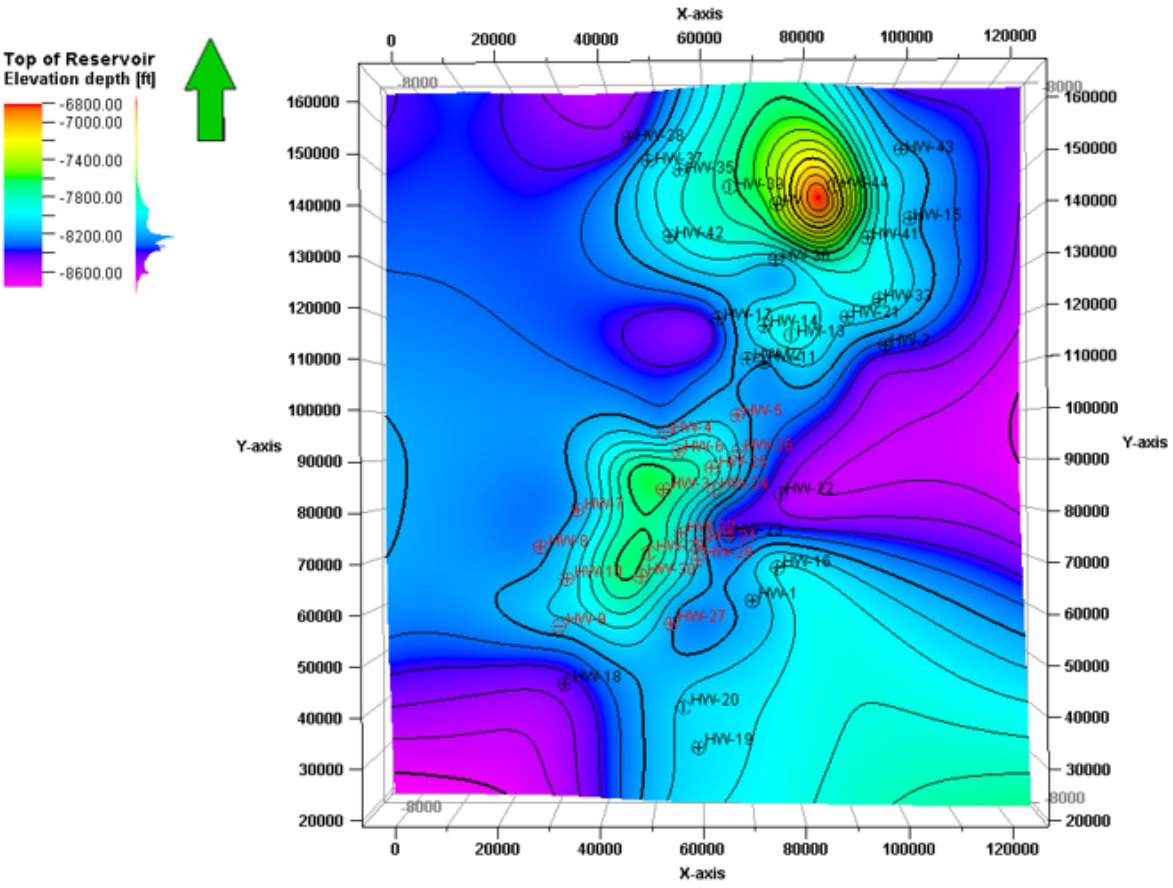

Figure 4: 3D view of the structure of the reservoir, displaying all available 43 wells, and highlighting 17 wells with logs in red.

2.1.2 Data cleaning and readiness

The project does not include any permeability logs. Therefore, the main input for finding a porosity-permeability relationship is the core data. The core data have data points above and below the reservoir; these points are removed as shown in the log presented in Figure 5. The first track is the core porosity followed by the core permeability bounded by the top reservoir and bottom of the reservoir; it can be seen that the data outside of the reservoir are very low and could negatively affect the relationship and underestimate the permeability to be modeled. Therefore, in the third track, the cleaned core porosity is followed by the cleaned core permeability where any points beyond the reservoir were removed to maintain the integrity of the reservoir. Also, in the last two panels there is a white circle that represents each core point taken every 0.5 ft, confirming that it covers the entire reservoir and ready to use for the petrophysical analysis.

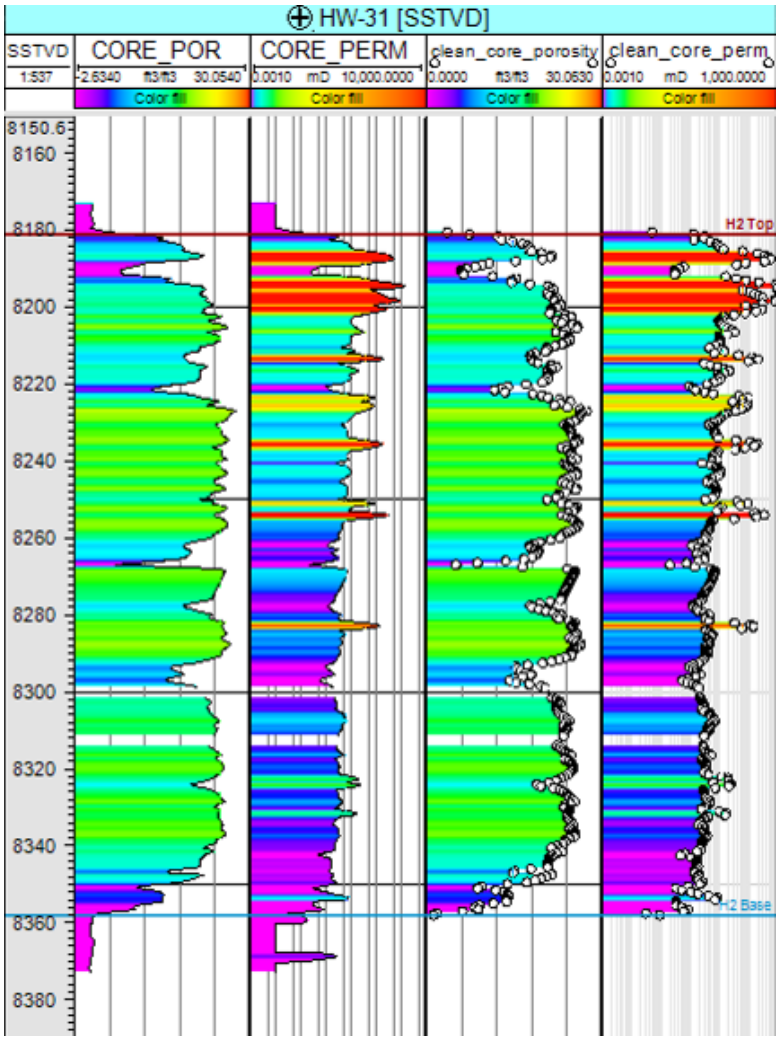

Figure 5: Well log for well HW-31, displaying in tracks core porosity, core permeability, clean core porosity, clean core permeability consecutively. And are bounded by the red line (top of reservoir) and blue line (bottom of reservoir) The first two tracks show data outside these boundaries hence, removed and cleaned to maintain reservoir integrity as they could underestimate the permeability model.

2.2 Petrophysical Analysis

2.2.1 Porosity and permeability relationship

As mentioned earlier there are no available permeability logs, therefore core data points were used to establish a relationship between porosity and permeability. The permeability values ranged from 0.01 millidarcies (mD) to 3080 mD showing high variability in the data set. When plotting permeability against porosity on a standard scale, there is no apparent linear relationship between them, as shown in Figure 6. Therefore, a logarithmic scale was applied to permeability values, as this method is useful for data with varying orders of magnitude, where it is compressed to identify trends. The logarithmic scale showed a better apparent log-linear relationship in Figure 7, which serves as the basis for this research and will be referred to as the base method in upcoming chapters. It is a reference for studying how the application of rock typing methods will have a porosity-permeability relationship per rock type that will influence reservoir properties, compared to the general relationship.

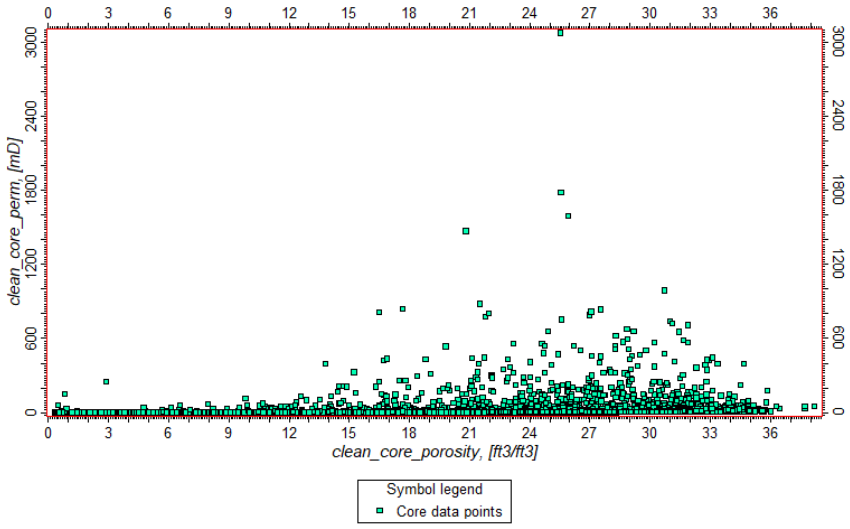

Figure 6: Cross plot of raw data for permeability and porosity measured in core plugs.

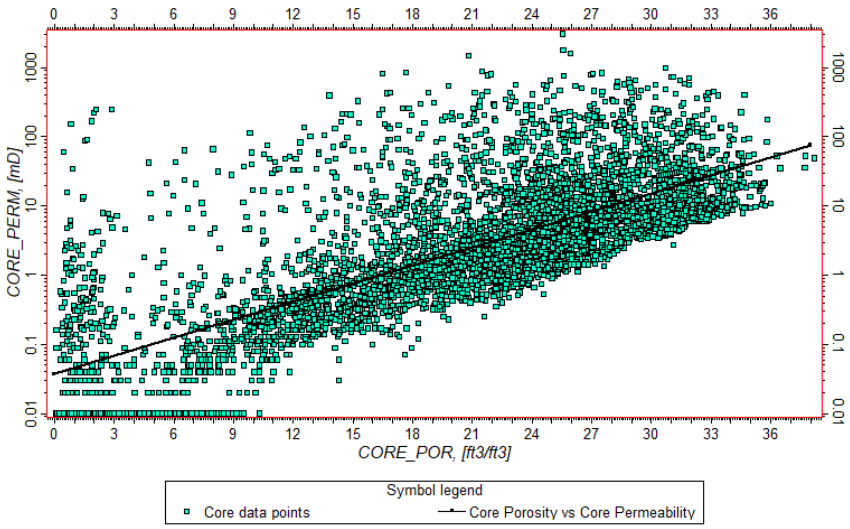

Figure 7: Cross plot of raw data for permeability and porosity measured in core plugs in logarithmic scale.

The linear trend in Figure 7 is represented in Equation 1.

$$\log(k) = 0.087 * \varphi - 1.431 \tag{1}$$

Where k is permeability and φ is porosity

2.2.2 Rock Typing

Winland R35 classification and Flow zone indicator rock typing methods were selected to be preformed in petrophysical analysis. As in carbonates, the effect of diagenetic processes is not captured by a simple correlation. Therefore, parameters for pore geometry and pore types are the most appropriate for static rock typing as the pore system conducts fluids by controlling the size and connectivity of the pore throats (Aliakbardoust and Rahimpour-Bonab, 2013).

Winland R35 Classification

The Winland R35 (Winland35) rock typing method is an empirical method named after the geologist Dale Winland (Rebelle and Lalanne, 2014). His method was further developed by (Kolodzie, 1980) and later by (Pittman, 1992), and has since been widely used in reservoir characterization(Rebelle and Lalanne, 2014). The method determines the pore-throat radius at 35% mercury saturation from the mercury injection capillary pressure (MICP) test indicating the naming of R35 (Ahmed, 2019). The capillary pressure is the pressure difference at the interface between two immiscible fluids; mercury and water, and has an inversre relationship with the pore throat size (Kadkhodaie and Kadkhodaie, 2022). Values of R gives an indication of pore throat size and their connectivity, as high values of R are related to better reservoir quality, where low values indicate poor quality or tighter parts of the reservoir. The Winland35 is expressed in Equation 2 (Rebelle and Lalanne, 2014).

$$\log R_{35} = 0.732 + 0.588 * \log k - 0.864 * \log \varphi \tag{2}$$

where R35 is the radius of the pores throat, k is the permeability and φ is the porosity.

After applying the equation, different ranges of the rock pore throat radius have been identified, with a minimum value of 0 and a maximum value of 120. These values were grouped into 4 types accroding to (Martin et al., 1997) in Figure 8 with different colors, the first type is the megaport flow unit that show the best reservoir quality, with values between 120 and 10 highlighted in beige, while the second type is the macroport that has less quality with values between 10 and 2 highlighted in brown, the third type is the mesoport that has values between 2 and 0.5 highlighted in gray, and the last type is the microport had a poor quality reservoir with values less than 0.5 highlighted in blue.

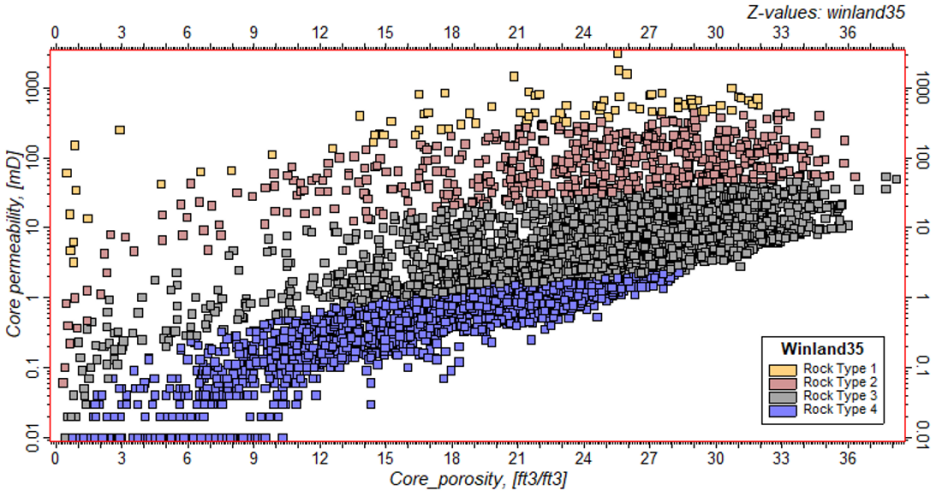

Figure 8: Cross plot of core porosity vs core permeability with Winland35 rock-types.

Flow Zone Indicator

The Flow Zone Indicator (FZI) is a method that, similar to Winland 35, correlates porosity and permeability to identify rock types based on flow units (Rebelle and Lalanne, 2014). It has two main parameters, the Reservoir Quality Index (RQI) and the effective porosity, the RQI is the ratio between permeability and effective porosity to measures the flow potential in the reservoir calculated using 3 (Rebelle and Lalanne, 2014):

$$RQI = 0.0314 * \frac{\sqrt{k}}{\varphi_e} \tag{3}$$

The FZI is calculated using 4 that is based on the ratio between RQI and the effective porosity. The method classifies the reservoir into different hydraulic units based on connectivity and pore type. An FZI with high values indicates a better quality rock in terms of connectivity and flow potential, and an FZI with low values indicate less quality and more limited flow potential.

$$FZI = RQI * \frac{1 - \varphi_e}{\varphi_e} \tag{4}$$

After applying these equations to the core data, a range of results for FZI values are obtained with a minimum value of 0.09 and a maximum value of 750. The rock types were classified according to these values into 5 types shown in Figure 9 to compare with Winland35. Starting from the top of the cross-plot, the first type is the better quality reservoir type with better flow potential that ranges between 750 and 10 highlighted in beige, the second type is between 10 and 2 highlighted in brown, the third type is between 2 and 1.5 highlighted in gray, the fourth type is between 1.5 and 0.5 highlighted in blue, and the fifth type is less than 0.5 which is poor in quality and limited in reservoir connectivity highlighted in yellow.

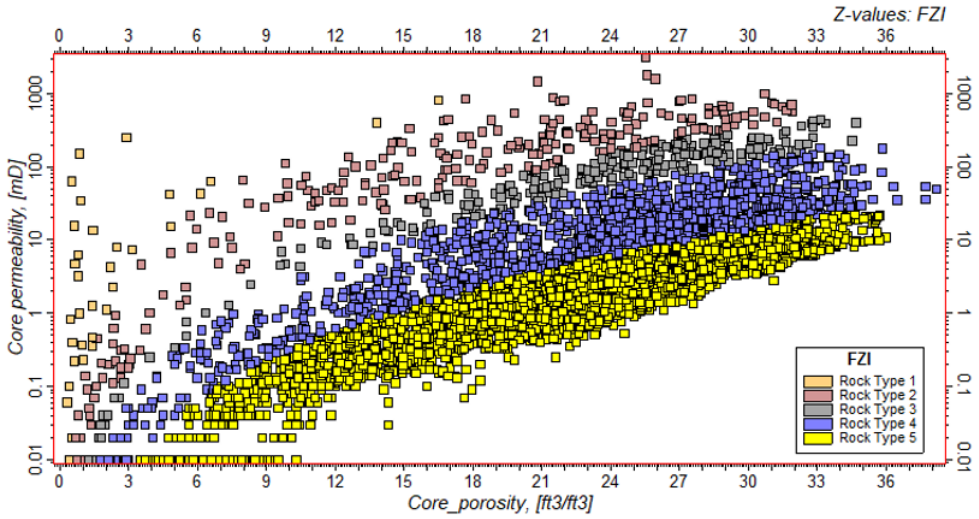

Figure 9: Cross plot of core porosity vs core permeability with FZI rock-types.

2.3 Static Modeling

The well tops and porosity well logs are used as input for the static model with the integration of the different methods applied for petrophysical rock characterization; base and rock typing methods.

2.3.1 Structural model

In order to build the static model, a structural framework is used to define the grid to be populated by the reservoir properties. The grid geometry is defined by top and bottom boundaries, cell size, vertical thickness of the cell, and layers going into the model based on the reservoir thickness. The well tops of the top and bottom reservoirs are used to create a surface map. The surface maps serve as input for the grid top and bottom boundaries in order to provide a conformable grid and capture any structural variations. Given the large area of the project, the grid cell increments in the x and y directions are set to 250 m, Due to the size of the area larger are chosen to account for the computational time for simulations. The reservoir has a maximum thickness of 197 m; therefore, 197 layers are created with a minimum vertical cell thickness of 1 m. The grid resolution parameters can be found in Table 1.

Area	13300 0m x 148250 m
Grid cells (nI x nJ x nK)	532 x 593 x 197
Grid nodes (nI x nJ x nK)	533 x 594 x 198
Total number of grid cells	62148772
Total number of grid nodes	62687196

Table 1: Grid resolution parameters.

As part of the grid quality check, geometrical modeling with three methods are used to test the quality on all the cells in the grid; Cell inside-out, cell apparent angle, and cell maximum internal angle.
Cell inside-out is a method to highlight any distorted cells in the 3D grid. It is significant for the accuracy of simulation to have good cell geometry instead of cells corners being inside out, which will result in negative cell values or errors in simulation. Figure 10(a) shows that there were zero cells with inside out corners, which means the cells are good. Cell angle calculates the deviation of the cell angle from 90°, with the apparent cell angle as the compass orientation of the cell shown in Figure 10(b) having a zero value, indicating that there is no deviation. The cell maximum internal angle is the angle between two edges within the cell with worst quality. There were more than 90% of cells with no deviation, while the rest showed a maximum deviation of 0.05°as shown in Figure 10(c). These methods validate the structural model showing no signs of distortion or major deviation in the cells, making it fit for the property population.

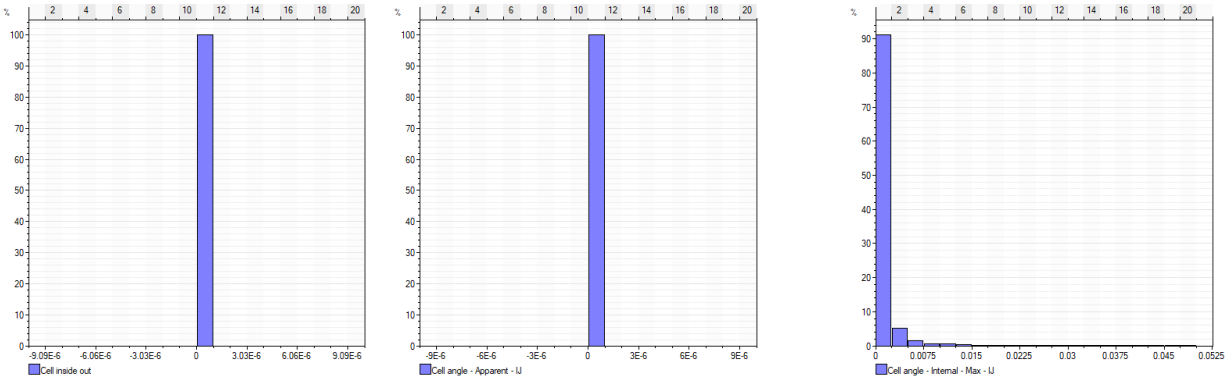

((a)) Cell inside-out histogram. ((b)) Apparent cell histogram. ((c)) Maximum internal cell angle histogram.

Figure 10: Geometrical Modeling Distributions.

2.3.2 Well log up-scaling

The main objective of upscaling the well log is to capture the well log data in the grid cells. This process is important in preserving the heterogeneity and fine layers in the large-scale model, as it is the main input for petrophysical property modeling that is used in simulation. Therefore, a number of methods are tested to honor the log data. For the porosity log, a series of methods are used and evaluated, arithmetic, midpoint, and median. The median showed the best match to capture the log data in Figure 11(a) . For the rock-type logs belonging to Winland35 and FZI, the most-of the method had the best match shown in Figure 11(b) and 11(c). These methods were evaluated based on the histogram match of the well log with the upscaled logs.

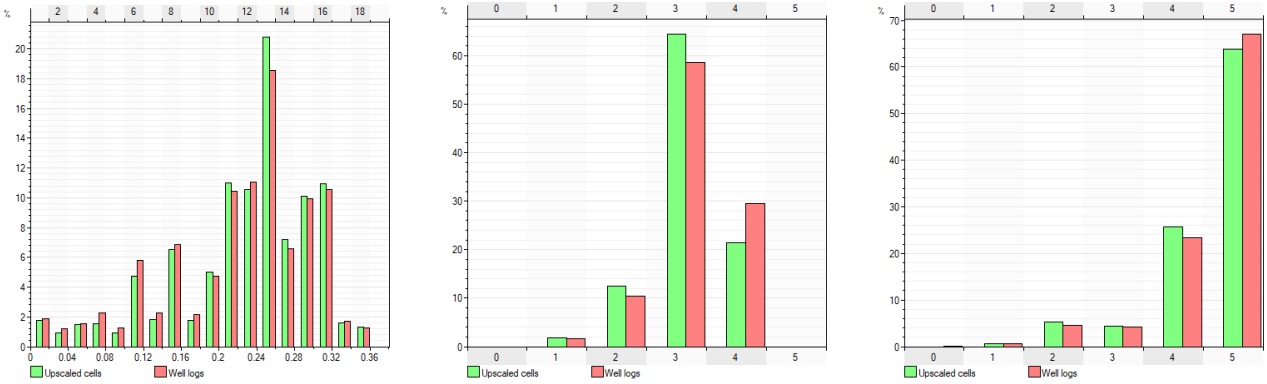

((a)) Histogram of upscaled log against the well log for porosity.

((b)) Histogram of upscaled log against the well log for Winland35 rock types.

((c)) Histogram of upscaled log against the well log for FZI rock types.

Figure 11: Histograms of the upscaled log in red against the well log in green.

2.3.3 Porosity Modeling

Sequential Gaussian simulation (SGS) method is used to create the porosity models, as it provides multiple realizations that allow to cover a range of uncertainties. The method forces the data into a normal distribution using a normal score transformation and assigns the transformed data point to the simulation grid (Ghojeh Beyglou, 2021). Then, it uses random paths from the grid nodes and uses simple kriging to estimate the random value for porosity extracted from the Gaussian probability distribution assigned to the grid cell (Ghojeh Beyglou, 2021). This process is repeated sequentially, and the randomness of this process allows to generate multiple realizations that can be utilized in performing uncertainty analysis. The semivariogram is a data analysis tool that shows data points with respect to distance and provides a spatial correlation that will define the spatial boundaries of the correlation in the model. This is performed on the upscaled logs to determine the lateral (horizontal range) and vertical continuity (vertical range) of the reservoir. It is used to set the semivariogram ranges that go into the property model. To obtain the best ranges, the direction of the available well log data is important to determine the horizontal range continuity of the data; it is set to 45° as seen by the direction of the cluster of wells in Figure 41(b). The number of lags represents the number of points to be correlated, and the lag distance is the distance between two points (Ringrose and Bentley, 2016). The bandwidth is used for the sampling configuration, as it limits the number of unreasonable pairs association and maximizes the reasonable pairs (Deutsch, 2015).
Table 2 shows the values of the semi-variograms for the vertical range, major horizontal range, and minor horizontal range for the porosity model. Figures of these correlation can be found in Appendix A.

Vertical range	Major horizontal direction	Minor horizontal direction
75	22000	18500

Table 2: Variogram ranges for porosity model

The model showed a distribution similar to that for the well logs and upscaled logs in Figure 12.

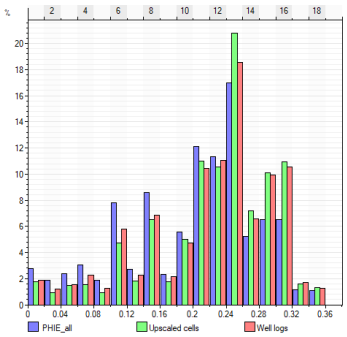

((a)) Histogram showing the upscaled log, well log and model for porosity.

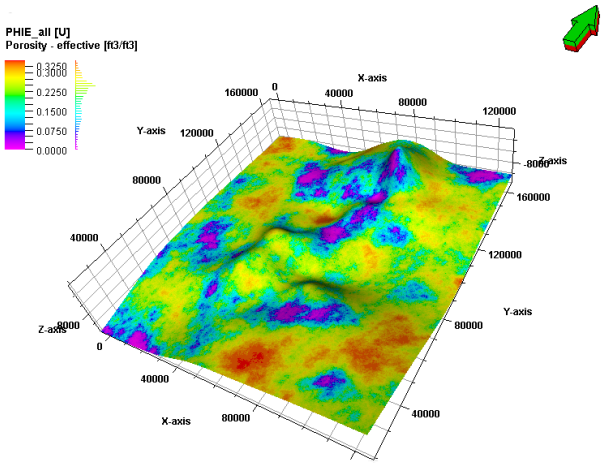

((b)) Base case porosity model.

Figure 12: Porosity model and histogram.

2.3.4 Rock Type Modeling

For the rock type modeling, a similar approach to facies modeling is implemented using Sequential Indicator Simulation (SIS). This method is widely used for discrete properties such as facies and rock type. and follows the same process as SGS. But instead of extracting from a Gaussian distribution, it assigns random indicators (rock types) while still adhering to the proportions of these rock types in the data. Semivariogram analysis is also performed for rock-type models and ranges can be found in Table 3. Similarly to the porosity model, the rock-type models in Figure 13 and 14 showed a distribution similar to the well logs and the upscaled logs.

Rock-type model	Vertical range	Major horizontal direction	Minor horizontal direction
Winland35	27	18600	12000
FZI	40	20000	14000

Table 3: Variogram ranges for rock-type models

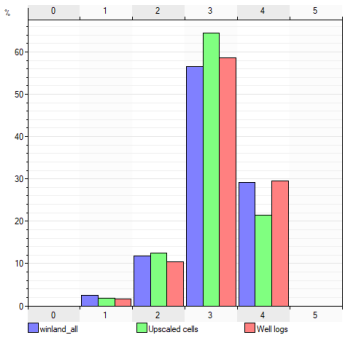

((a)) Histogram showing the upscaled log, well log and model for Winland35 rock types.

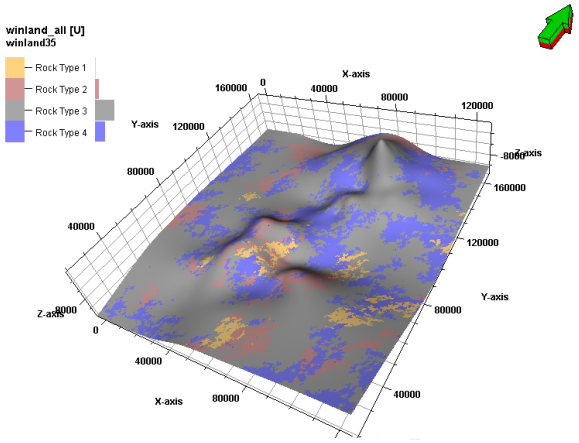

((b)) Winland35 rock type model

Figure 13: Winland35 rock type histogram and model

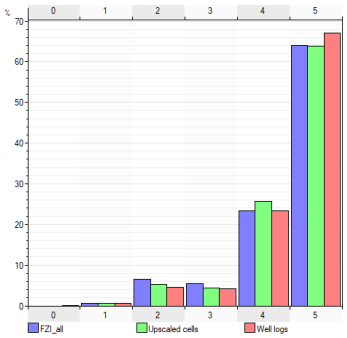

((a)) Histogram showing the upscaled log, well log and model for FZI rock types.

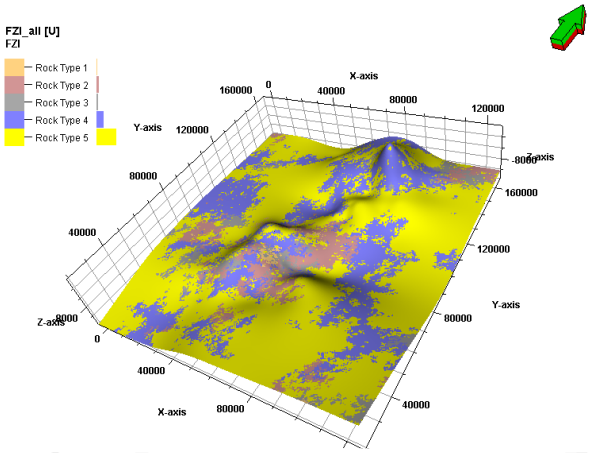

((b)) FZI rock type model

Figure 14: FZI rock type histogram and model

2.3.5 Permeability Modeling

The main method to model permeability is to transform the porosity models using the general relationship or the rock types relationships within the method. The data of each rock type is imported into excel to find the relationship between porosity and permeability by finding the best fit for correlation and using the different equations as input in Petrel. Initially, the permeability model is set to equal the rock type model, and then each rock type was transformed by using the porosity model and equation extracted per rock type, where it was bounded by the permeability range in the rock type to eliminate any over- or under-estimations.

For the Winland35, four equations were extracted as seen in Equations 5, 6, 7 and 8. Consecutively with the crossplots in Figures 15(a), 15(b), 32(b) and 15(d).

$$\text{Rock Type 1} : \text{k} = 1889.7 * \varphi^{0.98} \tag{5}$$

$$\text{Rock Type 2} : \text{k} = 577.7 * \varphi^{1.39} \tag{6}$$

$$\text{Rock Type 3} : \text{k} = 55.8 * \varphi^{1.64} \tag{7}$$

$$\text{Rock Type 4} : \text{k} = 25.2 * \varphi^{2.20} \tag{8}$$

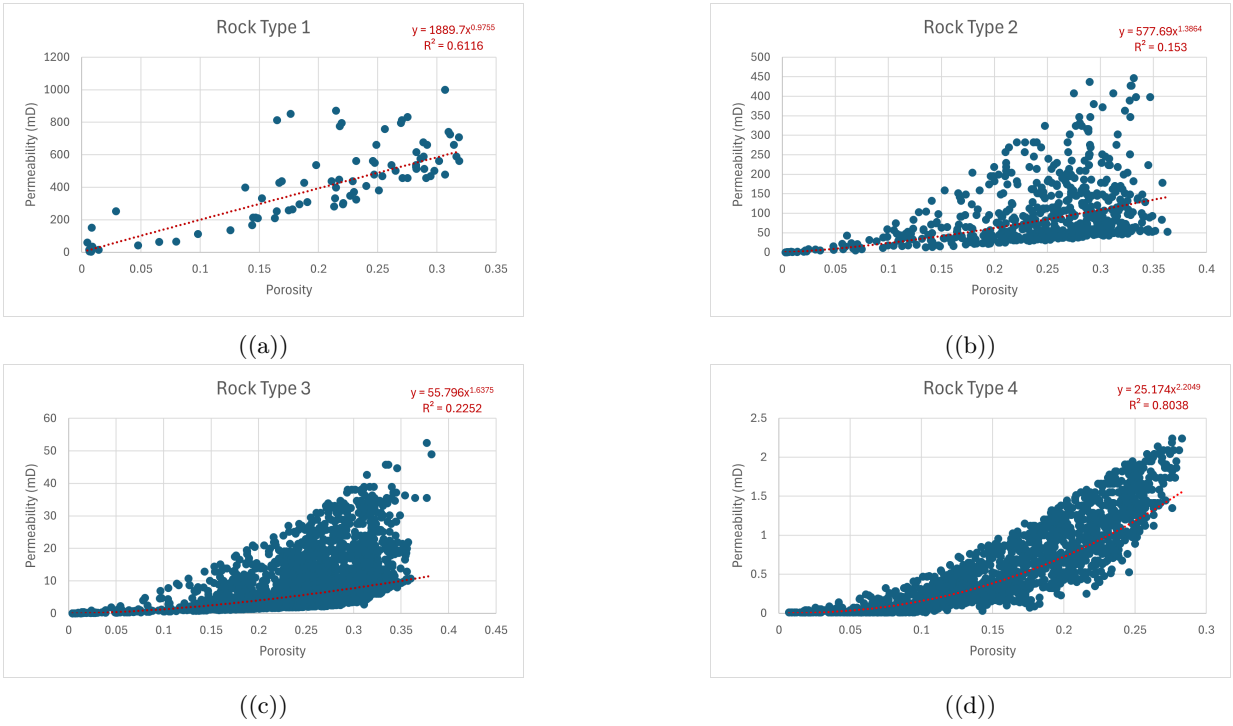

Figure 15: Winland35 porosity-permeability crossplot per rock type.

For FZI, five equations are extracted as seen in Equations 9, 10, 11,12 and 13. Consecutively with the crossplots in Figures 16(a), 16(b), 16(c), 16(d) and 16(e).

$$\text{Rock Type 1} : \text{k} = 66477 * \varphi^{2.41} \tag{9}$$

$$\text{Rock Type 2} : \text{k} = 21839 * \varphi^{2.96} \tag{10}$$

$$\text{Rock Type 3} : \text{k} = 9119.5 * \varphi^{\ 3.24} \tag{11}$$

$$\text{Rock Type 4} : \text{k} = 1333.4 * \varphi^{3.12} \tag{12}$$

$$\text{Rock Type 5} : \text{k} = 500.3 * \varphi^{3.68} \tag{13}$$

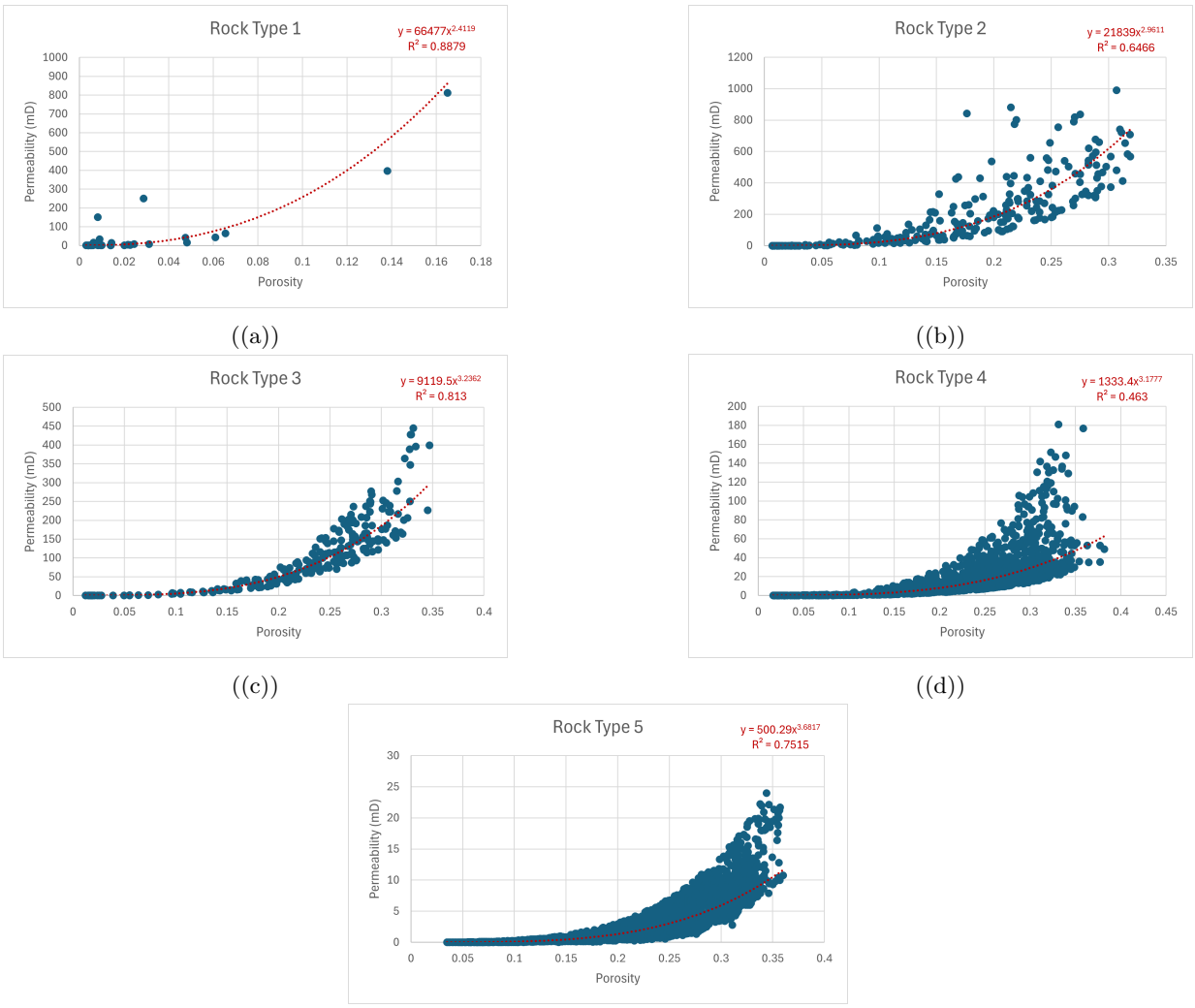

Figure 16: FZI porosity-permeability crossplot per rock type.

2.3.6 Cross Validation

Resampling is applied to the data set, with the use of 80% of available wells for training and remaining 20% wells for testing. This approach is repeated to produce 5 distinct cases of resampling based on different well combinations used for validation. Each case has a porosity model transformed to 3 permeability models used for cross-validation in static modeling and simulation illustrated in Figure 17 . Consequently, a total of 15 permeability models are used for cross-validation.

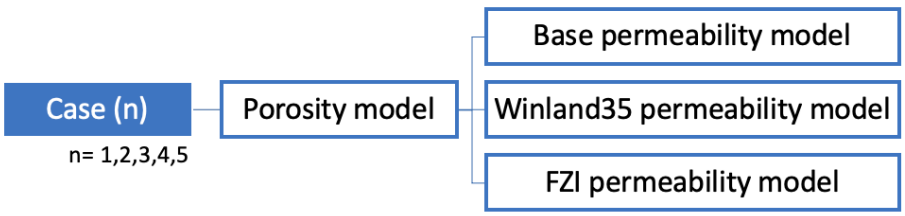

Figure 17: Diagram showing the transformed permeability models for all 5 case, resulting in a total of 15 models (5x3).

2.3.7 Uncertainty Analysis

As mentioned in the porosity modeling section, SGS provides multiple realizations. This can be utilized in performing an uncertainty analysis for the models. For this research, the analysis is performed on the porosity model only. Five realizations are created by changing the global seed while keeping the same parameters for modeling.
Figure 18 shows the porosity distributions for the different realizations. The distribution does not show great differences when it comes to porosity values. But the differences are found in the statistics for these realizations in Table 4, as it has different values for mean and standard deviation. Although only global seed was changed for the same model, this caused changes in the distribution of porosity as can be seen in the different ranges of mean and standard deviation.

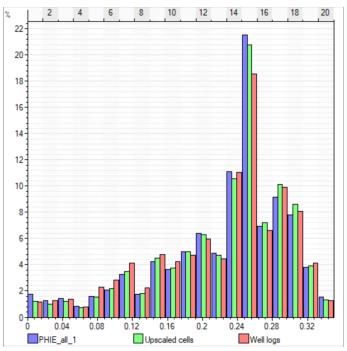

((a)) Realization 1

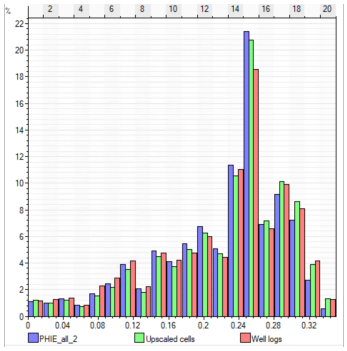

((b)) Realization 2

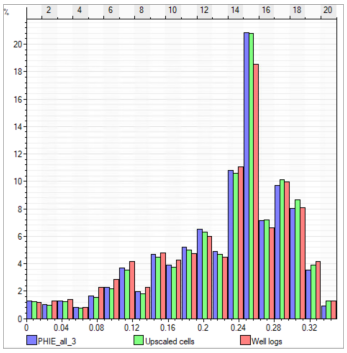

((c)) Realization 3

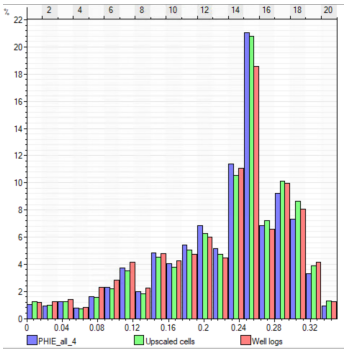

((d)) Realization 4

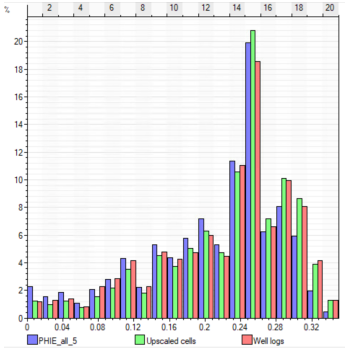

((e)) Realization 5

Figure 18: Porosity histograms for the realizations

Realization	Global seed	Mean	Standard deviation
1	2272	0.2232	0.07406
2	1705	0.2199	0.0712
3	3333	0.2227	0.0725
4	222225	0.2220	0.0709
5	369	0.2092	0.0767

Table 4: Realizations statistics

2.4 Dynamic Modeling and Simulation

2.4.1 Reservoir grid and parameter

The property models are exported from Petrel as a rescue file. It is important to note that the area is large and due to time limitations the area was reduced to 53x10^3 km^2 focusing on the anticline with the thickest layers present in the reservoir that is surrounded by wells with well logs as shown in Figure 19 with grid resolution parameters in Table 5.

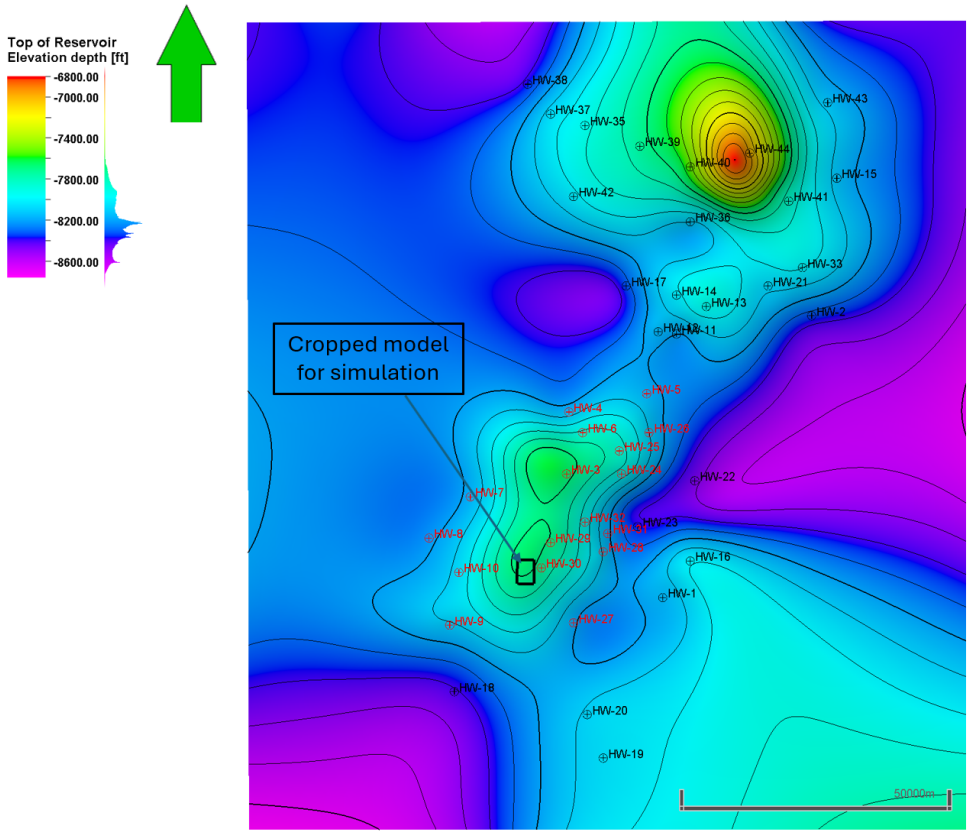

Figure 19: Structure map of top reservoir showing the selected area for simulation in black polygon.

Area	7250 m x 7250 m
Grid cells (nI x nJ x nK)	29 x 29 x 197
Grid nodes (nI x nJ x nK)	30 x 30 x 198
Total number of Grid cells	165677
Total number of grid nodes	178200

Table 5: Grid resolution parameters for cropped model.

Later, the rescue files are imported to CMG Builder software as an input for the reservoir grid. The properties of the grid are used to set the porosity and permeability grids. For the permeability grid, the i,j,k directions are set with the same grid for simplicity, making the permeability isotropic. This means that the reservoir grid assumes a flow equal in all directions and does not give an accurate representation of flow variability related to heterogeneity in the vertical and horizontal directions, leading to uncertainties in flow behavior and reservoir capacity. The reservoir standard condition parameters are summarized in Table 6 for rock compressibility, reference pressure, and temperature. There is no literature related to rock compressibility in the Upper Kharaib member; therefore, a rock compressibility is based on a nearby carbonate oil field in Iran that was established at 1x10^{-6} 1/KPa (Hashemi et al., 2012). It is an important parameter to calculate the compaction that the rock undergoes as a result of pressure changes, which will help in pressure management to avoid leakages and ensure the containment of CO_2 (Fanchi, 2005). To account for the properties of the fluid and the rock under standard conditions, it is necessary to assume atmospheric conditions for the temperature pressure, which was the default value in Builder as 25°and 101.3 KPa (Pettersen, 2006).

Rock compressibility	1x10^{-6} 1/KPa
Reference temperature	25 C°
Reference pressure	101.3 KPa

Table 6: Reservoir standard condition parameters

2.4.2 Relative permeability

The model regards the reservoir as a saline aquifer with relative permeability curves sourced from CMG defaults due to the lack of literature review providing relative permeability curves for carbonate aquifers. In Figure 20(a), the relative permeability curve of the water saturation assumes no residual water saturation and can be seen for the gas permeability curve in Figure 20(b). These curves are not realistic, as water is typically retained in small pores, but for simplicity, it is assumed that CO_2 will fully saturate the reservoir. The capillary pressure, which is the difference in pressure at the interface between gas and water, has been excluded, further simplifying the model.

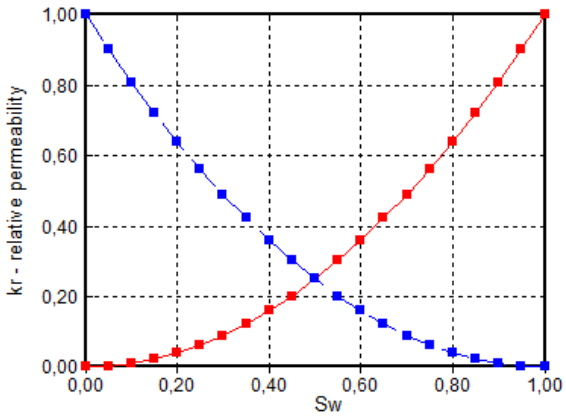

((a)) Krg vs. Sw relative permeability curve.

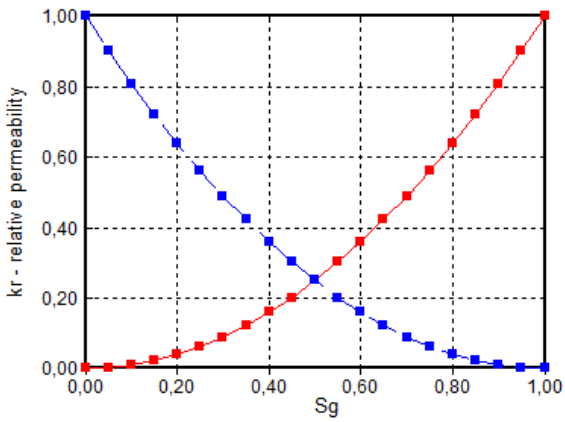

((b)) krg vs. sg relative permeability curve.

Figure 20: Relative permeability curves.

2.4.3 Initialization conditions

It is important to mention that the measurement units were converted to metric once imported to CMG. The top of the reservoir is at 7888 ft in Petrel and is converted to 2337 m in CMG. Initially, it is assumed that the reservoir is in hydrostatic equilibrium where the water table is set at 2000 m, placing it above the top layer of the reservoir, making it full of brine. Since it is in hydrostatic equilibrium, the initial pressure of the reservoir was set to hydrostatic pressure calculated in equation 14.

$$\mathrm{P} = \mathrm{g} * \rho_f * \mathrm{d} = 9.8\ \mathrm{m/s^2} * 1025\ \mathrm{kg/m^3} * 2337\ \mathrm{m} = 23499119.25\ \mathrm{kg/s^2 m} \approx 23500\ \mathrm{KPa} \tag{14}$$

Where g is gravity, ρ_f is the fluid density which is brine at 1025 kg/m3 and d is the reference depth of the reservoir at 2337 m.

Another condition is the reservoir temperature to account for the phase change that CO2 undergoes as the density changes with temperature and pressure, and it was calculated in equation 16 (Tiab and Donaldson, 2012).

$$\mathrm{T} = \mathrm{T_s} + \mathrm{G} * \mathrm{D} = 25\ \mathrm{C°} + (11\ \mathrm{C°}/304.8\ \mathrm{m}) * 2460\ \mathrm{m} = 113.8\ \mathrm{C°} \tag{15}$$

T_s is the surface temperature at 25 C°, D is the depth of the reservoir at 2460 m, G is the geothermal gradient for the Upper Kharaib reservoir at 11C/ 304.8m (Ehrenberg et al., 2020).

2.4.4 CO_2 injection well

The injection well was set at the same location for all scenarios, at the top of the anticline structure shown in Figure 21(a) . The well perforates through all of the 197 layers in the reservoir shown in Figure 21(b). The injection period was established for 50 years with the target injection of 1 million ton of CO_2 ($MtCO_2$) per year, and the monitoring period was established for 50 years to observe the behavior of the plume and the pressure of the reservoir after the well was shut.

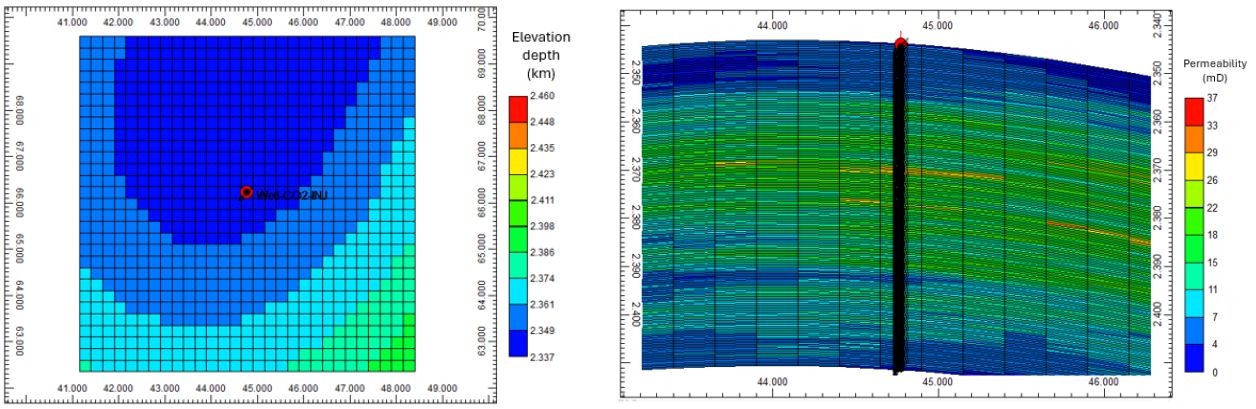

((a)) Grid top structure showing the well location for CO_2 injection well on top of the structure.

((b)) cross section of permeability grid showing the perforation points for CO_2 injection well.

Figure 21: Well location and perforation points for CO_2 injection well in Base method model case(all wells).

After placing the well and perforation points, the injection pressure for a target 1 $MtCO_2$ per year was found as following:

$$\text{Injecton} = \frac{\text{Targeted mass}}{\text{CO}_2 \text{ density}} * \frac{1}{\text{Number of days}} = \frac{1 * 10^9 \text{ kg}}{1.98 \text{ kg/m}^{-}3} * \frac{1}{365 \text{ days}} = 1383700 \text{ m}^3/\text{day} \tag{16}$$

Where CO_2 density is 1.98 kg/m^{-3} at surface condition since the injection pressure is the surface gas rate m^3/day.

It is important that the injection pressure does not reach the overburden pressure, therefore, the lithostatic pressure along with the fracture pressure gradient are used as the bottom hole pressure (BHP) in Equation 17 to avoid any fractures or leaks that can cause CO_2 leakage (Crumpton, 2018). In order to find the lithostatic pressure maximum depth at 2460 m and sand density is needed. The density log showed that the sand density ranges from 2080 kg/m^{-3} to 2790 kg/m^{-3}, with 2265 kg/m^{-3} being the highest in the distribution value, therefore, it was used as the sand density.

$$\text{BHP} = 0.7 * \text{g} * \rho_{litho} * \text{depth} = 0.7 * 9.8 \text{ m/s}^2 * 2265 \text{ kg/m}^{-3} * 2460 \text{ m} = 38223 \text{ KPa} \tag{17}$$

2.4.5 Boundary condition

CMG assumes a closed boundary for reservoir models, therefore, a volume modifier is placed at the vertical boundary of the models to simulate an infinite aquifer. The volume modifier is set at 10,000 pore volume multiplier, as it is the common factor for aquifers at basin level (Ghomian et al., 2024). Placing the multiplier only at the far edge will cause an aggregation of the pore volume. To avoid this, (Ghomian et al., 2024) suggests gradationally distributing the multipliers at the edges of the reservoir to mimic the behavior of the reservoir. In this project the multipliers are placed in a gradual increase in the six cells, only three are seen in Figure 22(a) due to the coloring scale, since the first three cells are below 667. However, with the use of this large number of multipliers, the reservoir capacity is overestimated (Ghomian et al., 2024). Therefore, a transmissibility reduction multiplier is applied to obtain a more reasonable capacity. To avoid transmissibility to the top and bottom of the reservoir (I-direction), the transmissibility multipliers in Figure 22(b) are also applied in a gradual increase, but due to the color scale in CMG only those with 0.0001 are shown. Similarly, the transmissibility multipliers are applied to the horizontal edges of the reservoir (J-direction) in Figure 22(c). In addition, transmissibility multipliers is applied to the vertical flow between the layers at the edges (K-direction) in Figure 22(d). By combining volume modifiers and transmissibility reductions, a more reasonable reservoir behavior is achieved.

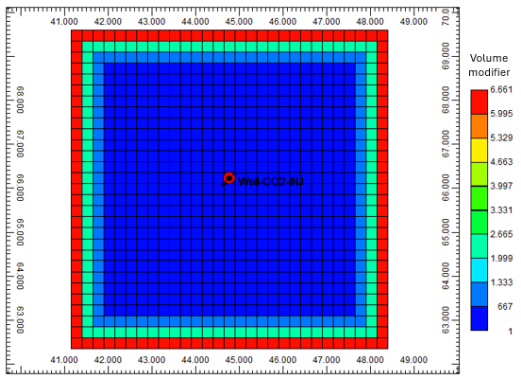

((a)) Volume modifier grid.

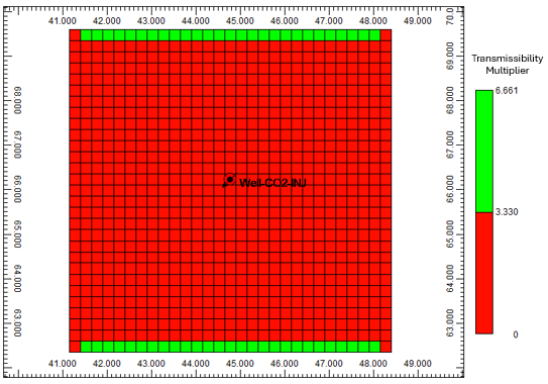

((b)) Transmissibility grid in the I-direction.

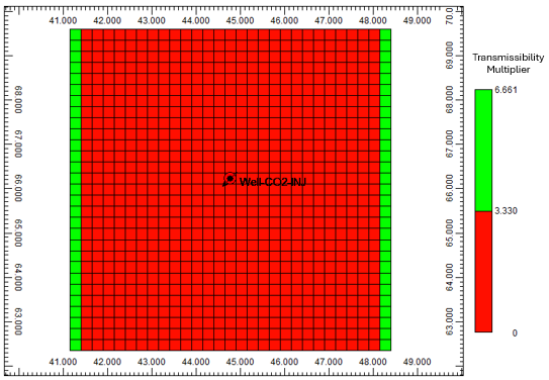

((c)) Transmissibility grid in the J-direction.

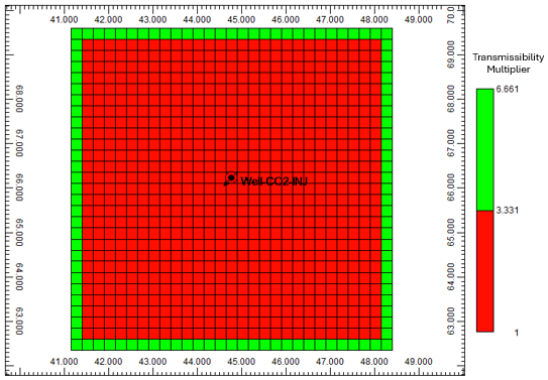

((d)) Transmissibility grid in the K-direction.

Figure 22: Boundary condition grids.

3 Results and Discussion

3.1 Static modeling

In static modeling, cross-validation cases were created based on different well combinations in Figure 23. The wells highlighted in red have porosity logs, therefore, the analysis will focus on their distribution in each case and their corresponding porosity distribution.

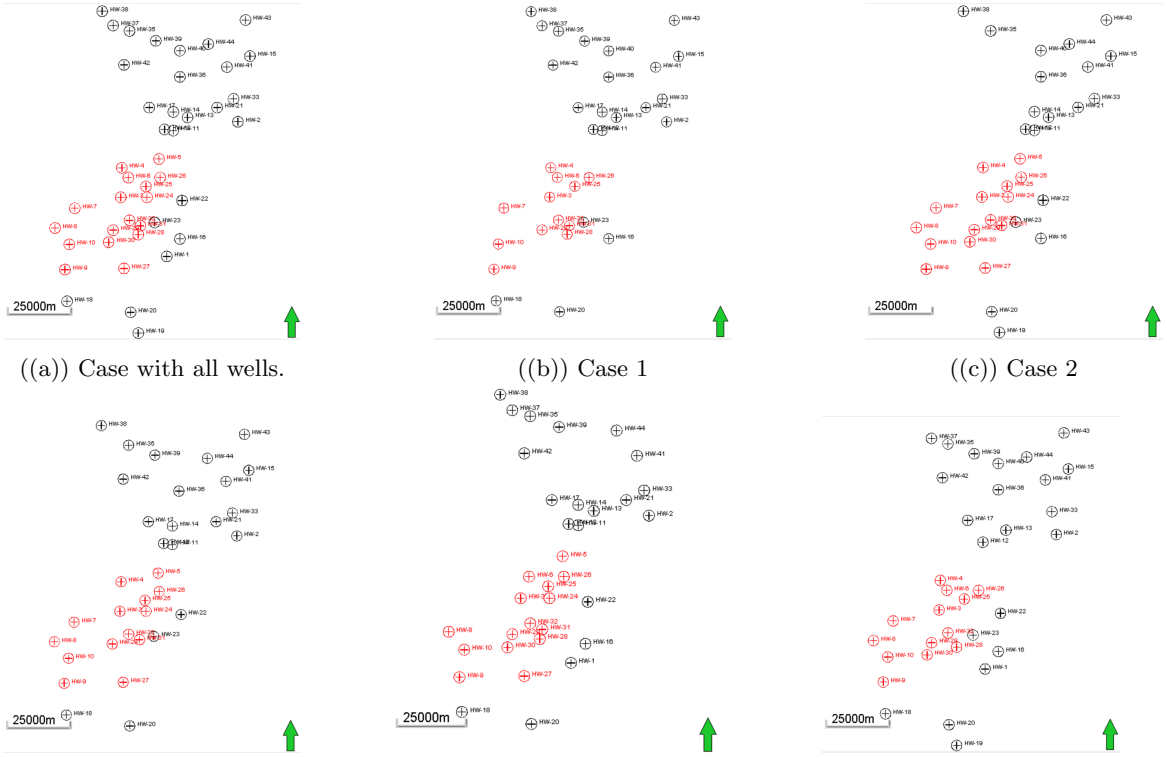

((a)) Case with all wells. ((b)) Case 1 ((c)) Case 2

((d)) Case 3 ((e)) Case 4 ((f)) Case 5

Figure 23: Different cases of well combinations used for cross-validation

The porosity distribution for these cases is shown in Figure 24. The case with all wells in Figure 23(a) provides the best available representation of the porosity distribution in the reservoir, as it includes all available data (Figure24(a)). For cases 1 and 5, there is an even distribution for the red wells with log cluster (Figure 23(b) and 23(f)), but it excludes further wells like HW-5 and HW-17. The porosity distribution in both cases (Figure 24(b) and 24(f)) shows that porosity is somewhat evenly distributed, but when looking at the statistics in Table 7, it can be seen that the mean in both cases is high and the standard deviation is low compared to the case with all wells. The lower standard deviation is an indication of a bias toward higher values and an overestimate of areas away from the red well cluster due to poor well control resulting in a higher mean. Case 2 shows better well control as it includes the wells away from the cluster (Figure 23(c)) and a similar porosity distribution (Figure 24(c)) to case 1 and 5. Although it is similar in distribution, it has a lower mean and a higher standard deviation than cases 1 and 5, reducing the bias to high porosity values that results in a lower mean. For cases 3 and 4, both show similar well control (Figure 23(d) and 23(e)) and similar porosity distribution (Figure 24(d) and 24(e)) that is slightly overestimating the lower porosity values. This is reflected in their mean, as they have the lowest mean values of all five cases (Table 7). Case 4 has a higher mean than case 3 as it has a higher distribution for high porosity values and lower standard deviation. All cases have the same approach for upscaling and modeling, but the difference, is in the input well data because each case has different combination of wells resulting in differences in the porosity distributions, mean and standard deviation.

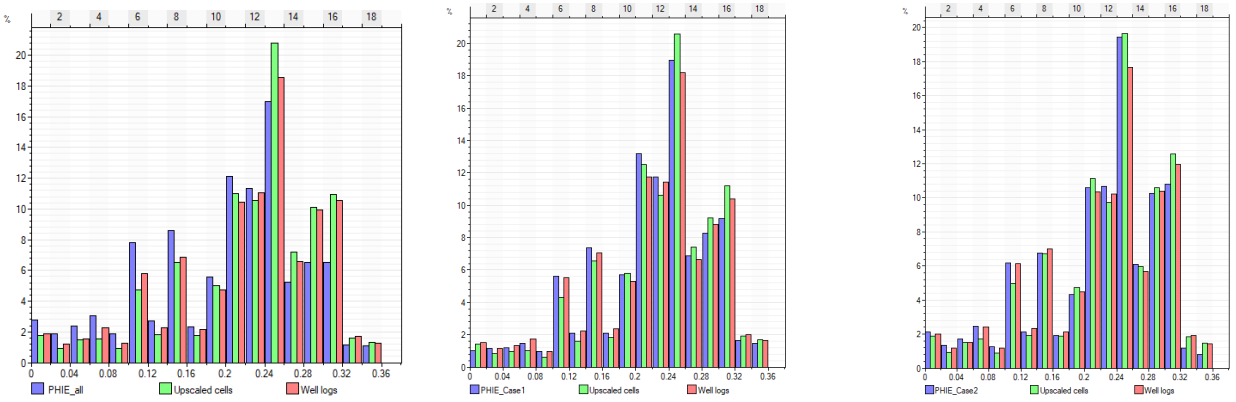

((a)) Case with all wells

((b)) Case 1

((c)) Case 2

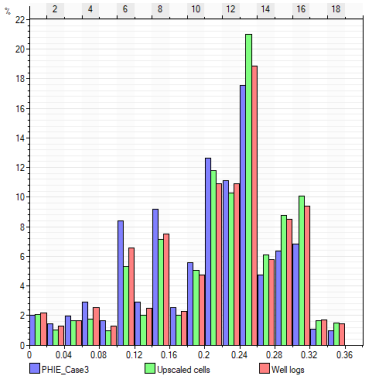

((d)) Case 3

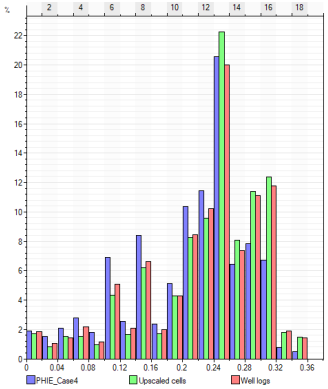

((e)) Case 4

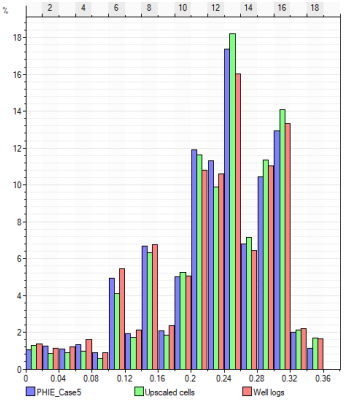

((f)) Case 5

Figure 24: Porosity histograms used for cross-validation

Porosity model	Mean	Standard deviation
All wells	0.2015	0.0796
Case 1	0.2220	0.0696
Case 2	0.2183	0.0765
Case 3	0.2035	0.0765
Case 4	0.2084	0.0755
Case 5	0.2275	0.0708

Table 7: Porosity models statistics

The differences in porosity distributions have direct implications for the permeability transformations applied in the three methods. Figure 25 shows the resulting permeability histograms for the base method in the different cases. Similarly to the porosity distribution, cases 1 and 5 have higher distributions for high porosity values and lower distributions for low porosity values as shown in Figure 25(b) and 25(f) with high mean in Table 8. Cases 3 and 4 show a higher distribution for low permeability values under 1 mD seen in Figure 25(d) and 25(e), and this is reflected in their mean as they are in the lower range mean of all cases in Table 8. The standard deviation for the permeability differs from that for the porosity. For example, cases 1 and 5 have lower standard deviations of all cases in the porosity distribution, but higher standard deviation than all in the permeability distribution, indicating that the poro-perm applied relationship also influenced the permeability distribution and statistics.

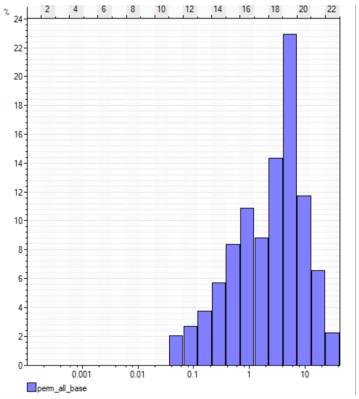

((a)) Case with all wells

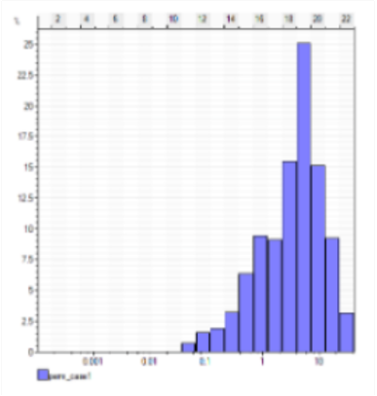

((b)) Case 1

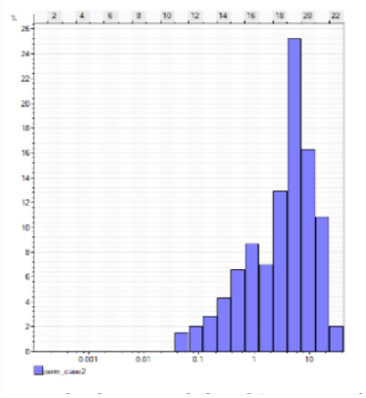

((c)) Case 2

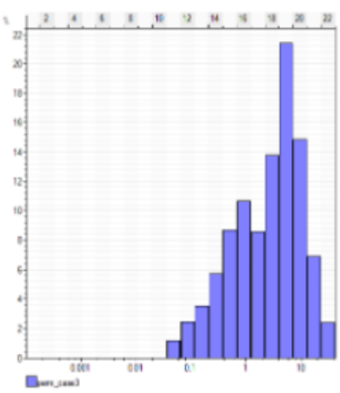

((d)) Case 3

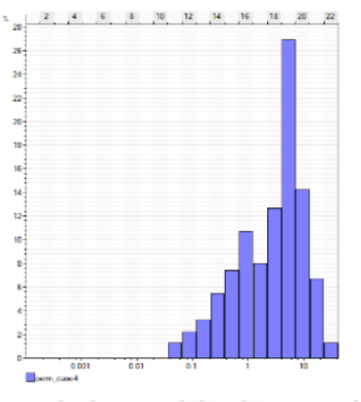

((e)) Case 4

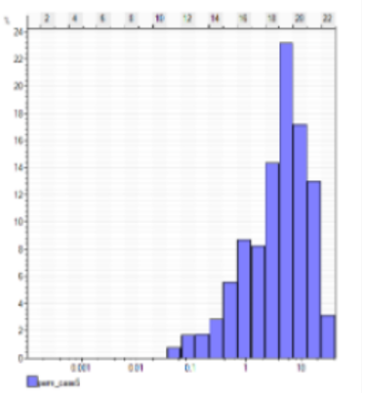

((f)) Case 5

Figure 25: Core permeability and 5 cases cross-validation for the transformed permeability using base method

Permeability model	Mean	Standard deviation
All wells	5.0414	5.8903
Case 1	6.1828	6.3447
Case 2	6.1616	6.0416
Case 3	5.0273	5.7925
Case 4	5.1639	5.2967
Case 5	6.8426	6.5840

Table 8: Base method transformed permeability models statistics

The base method and Winland35 show a similar order for the permeability in the different cases. Cases 1 and 5 have higher distributions for permeability values higher than 10 mD in Figure 26(b) and 26(f).Cases 3 and 4 show higher distributions for permeability values lower than 1 mD in Figure 26(d) and 26(e). Although the order of the permeability cases in Winland35 and the base method is significantly higher, the permeability values for Winland35 are significantly higher and are reflected in the mean and standard deviation values for the permeability cases of Winland35 in Table 9.

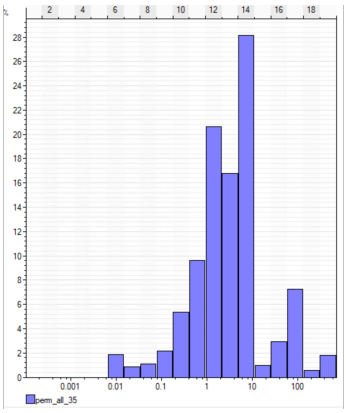

((a)) Case with all wells

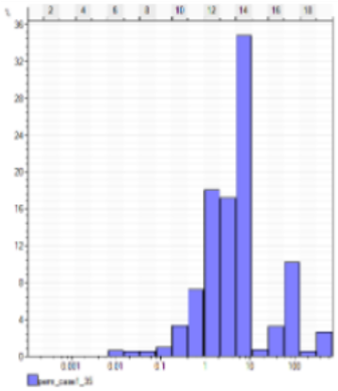

((b)) Case 1

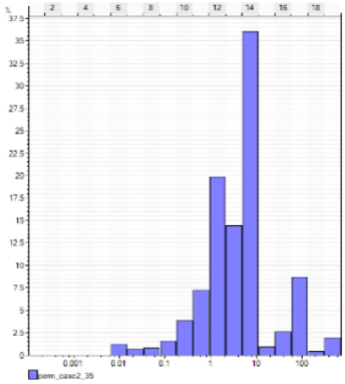

((c)) Case 2

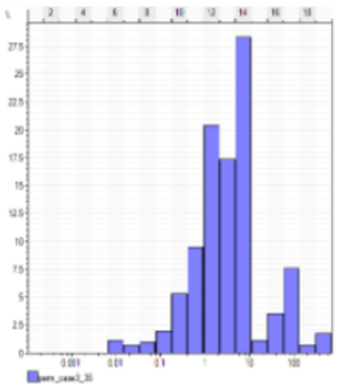

((d)) Case 3

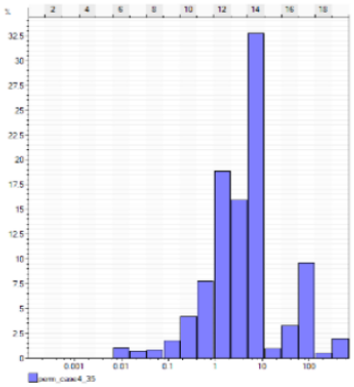

((e)) Case 4

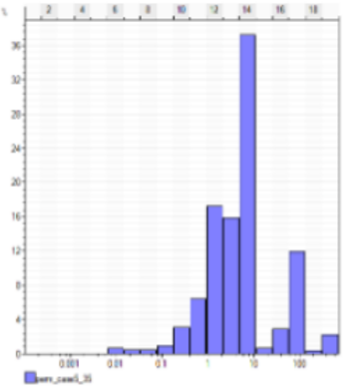

((f)) Case 5

Figure 26: Core permeability and 5 cases cross-validation for the transformed permeability using Winland35

Permeability model	Mean	Standard deviation
All wells	20.5114	68.7591
Case 1	27.6837	82.5079
Case 2	22.8980	73.1280
Case 3	20.8867	68.1783
Case 4	23.8112	72.959
Case 5	27.4947	78.1771

Table 9: Winland35 method transformed permeability models statistics

The transformed permeability models for the FZI cases show the highest permeability ranges compared to Winland35 and the base method shown in Figure 27. It also presents differences in the permeability distributions for the cases. Case 5 shows a lower distribution for permeability values higher than 10 mD (Figure 27(f)), while case 4 shows a higher distribution for permissibilities greater than 10 mD (Figure 27(e)). These distributions reflect in the mean value shown in Table 10 as case 4 has a higher mean than case 2 unlike in the previous methods. Similarly, case 5 has a lower mean than other cases. This shows that using different methods for petrophysical characterization, even within rock-typing itself between Winland35 and FZI, not only permeability ranges differ, but the statistics for the permeability models as seen in the mean and standard deviation also differ between the cases.

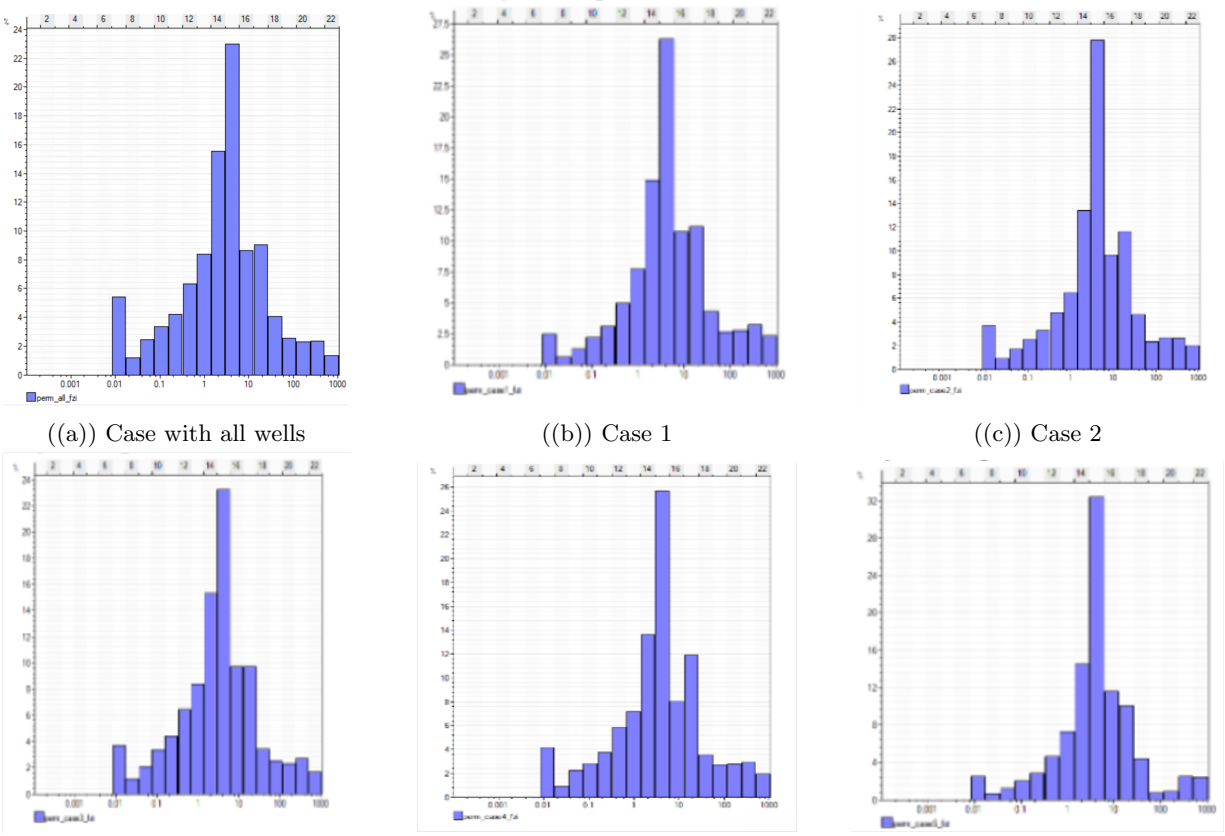

((a)) Case with all wells ((b)) Case 1 ((c)) Case 2

((d)) Case 3 ((e)) Case 4 ((f)) Case 5

Figure 27: Core permeability and 5 cases cross-validation for the transformed permeability using FZI

Permeability model	Mean	Standard deviation
All wells	28.4906	98.1675
Case 1	39.9123	123.0466
Case 2	34.9762	111.4203
Case 3	32.4133	108.4294
Case 4	36.2808	114.7507
Case 5	33.4398	118.8116

Table 10: FZI method transformed permeability models statistics

The cross-validation for the permeability models cases are used to find the generalizability of the different rock typing methods. The core permeability for the wells not included in the case are plotted against the synthetic permeability values for these wells in the cases that excluded these wells. Table 11 shows the different correlation coefficients for the different rock typing methods. The average for these coefficients is 0.01 for the base method, 0.29 for Winland35, and 0.29 for FZI. In general, FZI showed a generally higher correlation than other methods, except for case 4, and the base method showed a lower correlation than the other methods.

Case	Base method	Winland35	FZI
1	0.61	0.46	0.47
2	-0.2	0.28	0.41
3	-0.04	0.32	0.40
4	-0.38	0.06	-0.19
5	0.06	0.34	0.34

Table 11: Generalizability of the different rock typing methods

3.2 Simulation

The case with all wells and the cross-validation cases are run to evaluate the differences in the reservoir behavior, focusing on how the permeability models influence parameters such as bottom hole pressure, injection pressure, storage capacity, and plume migration. Furthermore, insights from the results are used to evaluate associated uncertainties in the rock typing method and permeability models, highlighting their effect on CO_2 storage.

The simulation was initially run on the 18 imported models including 6 porosity models and 3 different permeability models per porosity model. The runs were based on CO_2 injection rate (m^3 /day) and bottom hole pressure (KPa) as operation parameters. The operating time was set at 50 years of injection and 50 years of monitoring. The following are the results for the three cases with different permeability models with all wells.

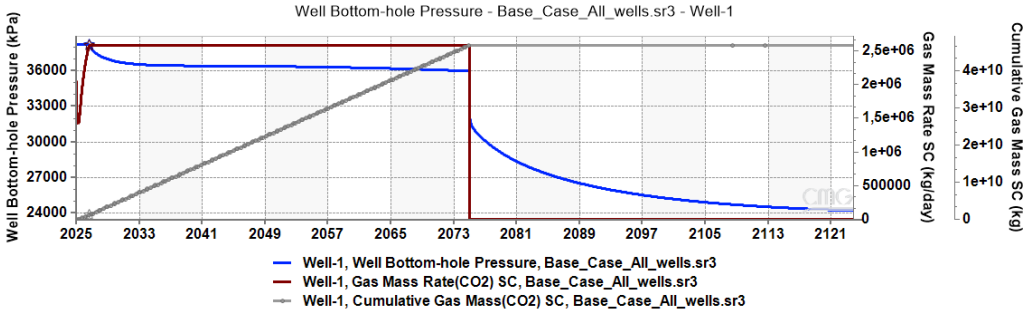

((a)) Base method

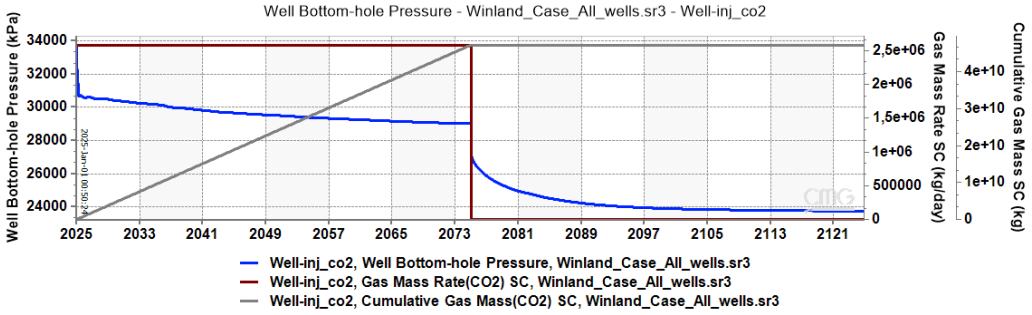

((b)) Winland35 method

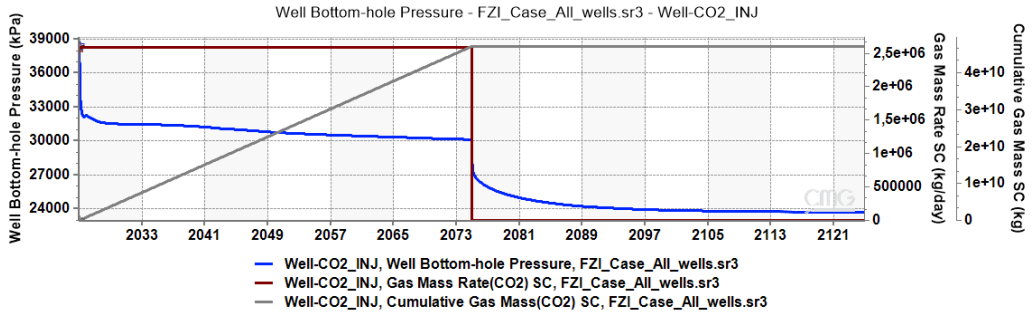

((c)) FZI method

Figure 28: Simulation results for surface gas rate for cases with all wells

As shown in Figure 28, the results included bottom hole pressure (blue), gas mass rate (red), and cumulative gas mass (gray). In the base method, the bottom hole pressure reaches the maximum pressure at the beginning of injection, as shown in Figure 28(a). While in the Winland35 and FZI, the bottom hole pressure never reaches the maximum pressure as seen in Figures 28(b) and 28(c). In order to understand the behavior of the bottom hole pressure, Darcys Law is used :

$$Q = \frac{KA}{\eta} * \frac{\Delta P}{L} \tag{18}$$

Where Q is injection rate, K is permeability, A is the cross sectional area, η is fluid viscosity and $\Delta P/L$ is the pressure gradient over the distance.

In this analysis, the area is considered constant. The pressure difference is the difference between the hydrostatic pressure, which is the initial reservoir pressure, and the fracture gradient, which is the maximum bottom hole pressure before fractures are induced (Burke, 2011).

From equation 18, the injection rate (Q) and the bottom hole pressure have a direct relationship. When the injection pressure is high in a reservoir with insufficient permeability, pressure starts to build-up around the well-bore and causes a higher bottom hole pressure (Birkholzer et al., 2011). This is seen in the base method that is low in permeability, as the injection rate is high, causing a pressure build-up and reaching the maximum bottom hole pressure. The Winland35 and FZI are considered more permeable than the base method, so the permeability allows the pressure to propagate away from the wellbore, never reaching the maximum bottom hole pressure. This implies that there is a potential to inject CO_2 at a higher rate.

Similarly to the injection rate, the fluid viscosity (η) has a direct relationship to the bottom hole pressure. When injecting CO_2 to the aquifer, the pressure around the well is higher and the viscosity of the brine increases as a result of this pressure. In addition, as the reservoir pressure increases due to injection, some of the CO_2 becomes soluble and increases in viscosity. These changes in viscosity create a flow resistance, ultimately creating a pressure build-up and increasing the bottom hole pressure. Although the change in brine viscosity is seen in Figure 29(b), it is negligible as the change is only 0.56%. Also, after the monitoring period in Figure 29(c), the viscosity decreases to the initial value as the reservoir stabilizes in pressure.

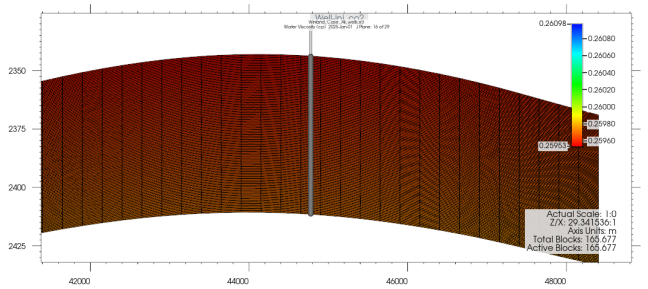

((a)) Brine viscosity before injection.

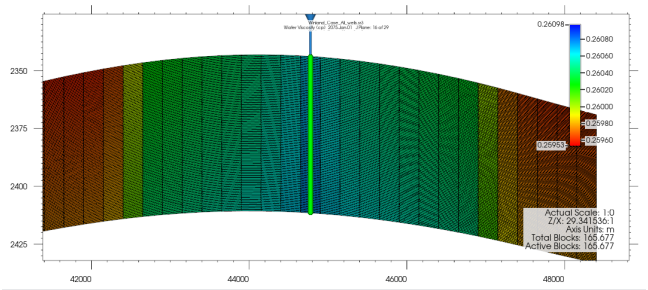

((b)) Brine viscosity after injection.

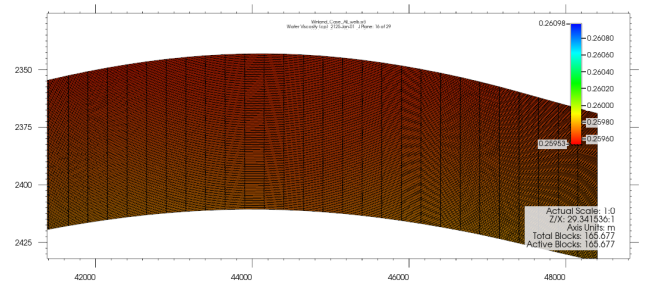

((c)) Brine viscosity after 50 years of monitoring.

Figure 29: Brine viscosity initially, after injecting, and after monitoring.

Another input that influences the bottom hole pressure is the perforation points and their location. A study by (Sun et al., 2024) shows how the perforation points and their location can affect the bottom hole pressure. He compared his approach of using multiple perforation points with (Chadwick et al., 2009) who used a single perforation point at the top of the reservoir and (Cinar et al., 2008) who also used a single perforation at the middle of the reservoir. His results show that placing the perforation point at the top resulted in the highest pressure build-up, followed by placing it in the middle of the reservoir, and finally having multiple perforation points showed the lowest build-up (Sun et al., 2024). In this research, the perforation points were placed in each layer of the 197 layers, allowing a better pressure distribution.

After the shut in of the well, the bottom hole pressure drops as CO_2 migrates away from the wellbore, therefore reducing the pressure build-up around the wellbore. Also, toward the end of the monitoring period the bottom hole pressure drops and stabilizes at the initial reservoir pressure, indicating that it reached the static pressure where the pressure has been distributed in the reservoir.

The winland35 and the FZI show similar storage of 47.23 $MtCO_2$ for case with all wells, while the base method stored 46.7 $MtCO_2$. The main driver of these changes is the permeability of the different models. The FZI has the highest values of permeability between 0.01 and 975 mD, followed by the winland35 with values between 0.01 and 675 mD, and finally the base method with values between 0.01 and 38 mD. These ranges definitely affect the CO_2 flow in the reservoir as higher permeability allows higher injection and less pressure build-up. It can be seen in Figure 28(a) where the base method showed a pressure build-up at the start of the injection as it reached the maximum bottom hole pressure due to the low permeability range.

Although the cumulative amount injected was 50 $MtCO_2$, a maximum of 47.23 $MtCO_2$ was stored. This mainly due for CMG reporting the cumulative gas mass as CO_2 stored in the supercritical phase. Figure 30 shows CO_2 supercritical moles and CO_2 soluble moles. The cumulative stored CO_2 (dotted line) is based on the supercritical CO_2 as it overlays it. Showing that the cumulative stored CO_2 is accounting only supercritical CO_2 and not the stored dissolved CO_2.
Another mass loss is the material balance error , these are errors related to convergence issues and time-step cuts (Avansi et al., 2019). Usually, GEMS provides an operation report that includes the material balance error during the simulation. The report states a 7.4170E-02% error for the case in Figure 30, which means that 37 tCO_2 is lost.

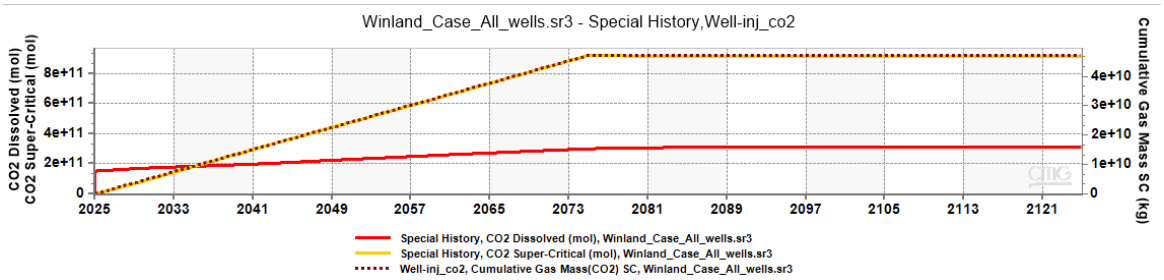

Figure 30: Winland35 simulation results displaying CO_2 in aqueous and supercritical phase.

Three additional simulations for the case with all wells for the different methods were run based on maximum bottom pressure injection to evaluate the maximum storage it can reach during 50 years. This is not an indication of their maximum storage capacity, but rather of the maximum possible injected CO_2 shown in Figure 31.

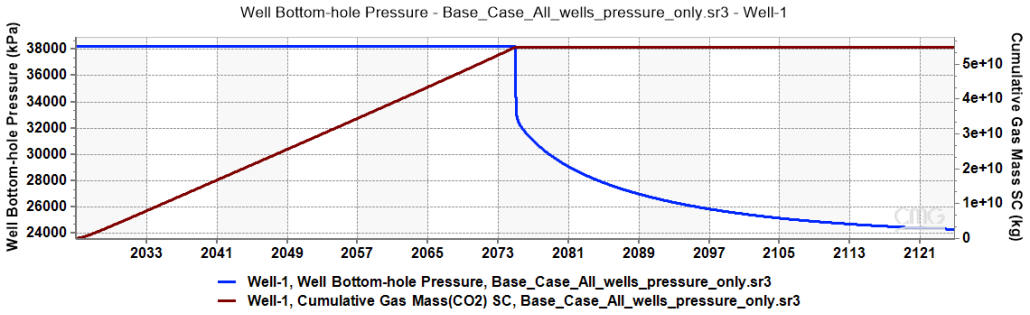

((a)) Base method

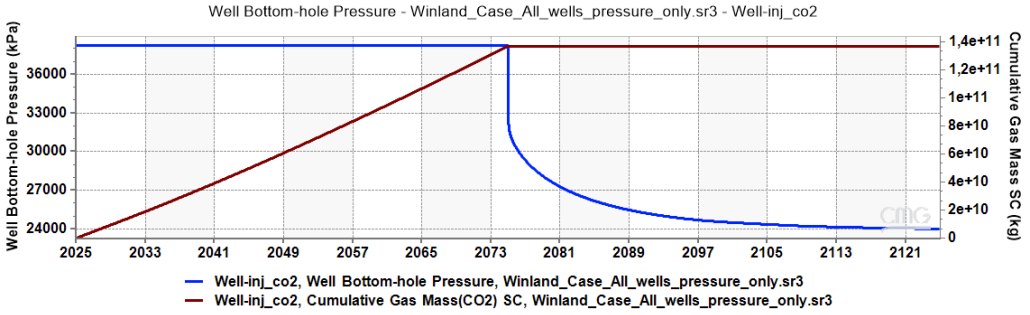

((b)) Winland35 method

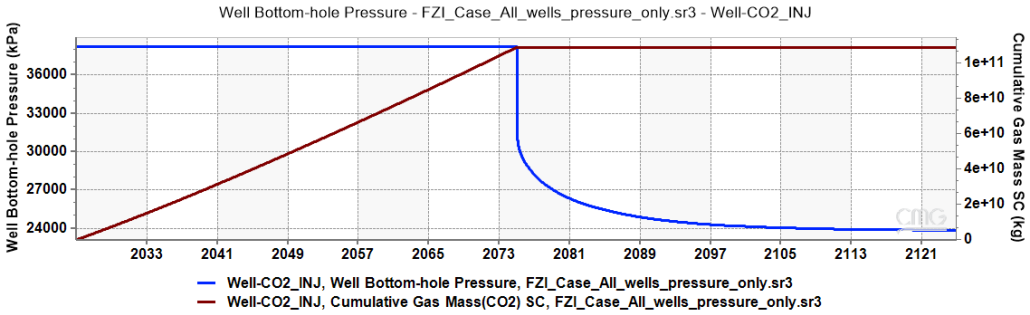

((c)) FZI method

Figure 31: Simulation results for maximum bottom hole pressure injection for cases with all wells

The Winland35 (Figure 31(b)) has the maximum storage of 136.7 $MtCO_2$, the FZI stored (Figure 31(c)) 109.1 $MtCO_2$, and the base method (Figure 31(a)) has the lowest amount stored 54.9 $MtCO_2$. These results displayed similar behavior to the previous simulation results after monitoring, as the bottom hole pressure drops after well shutin and eventually reaches the reservoirs initial pressure.

Although the FZI method has higher values of permeability, it stored less than the Winland35. Figure 32 shows the distribution of the permeability values, with the FZI method having more weight towards low permeability data. In general, it showed a higher distribution for the lower permeability range between 0.01 and 0.1 mD. Lower permeability values affect the flow of CO_2 by not allowing more intake.

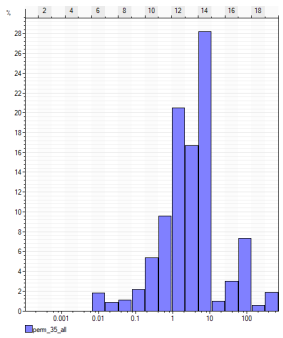

((a)) Permeability histogram for Winland35 transformed permeability model

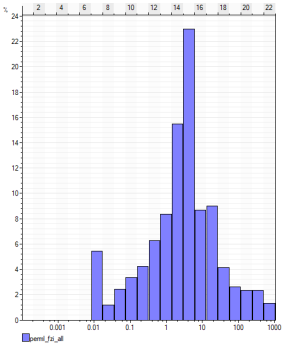

((b)) Permeability histogram for FZI transformed permeability model.

Figure 32: Permeability models histogram.

After analyzing the pressure behavior in the previous results, the focus continues to plume migration for these cases. Figure 33 shows the plume migration patterns after injection and monitoring period for the three different methods. Permeability plays a role in plume migration in the vertical and lateral pathways (Mackay, 2013). It is important to note that the same permeability is assumed in the I, J and K directions, making it isotropic. The affect of isotropy can be clearly seen in the symmetry of the plume shapes for all methods. The vertical movement of the plume in all methods shows an upward migration toward the structural trap after injection and a further migration after the monitoring period due to the buoyancy effect. The base method showed minimal upward movement after the monitoring period (Figure 33(b)), as it is lower in permeability, restricting flow. The Winland35 has a higher upward and lateral movement, as it was more permeable (Figure 33(d)). The FZI method has higher permeability than the other method and showed a higher upward movement of the plume in Figure 33(f), showing that plume migration is influenced by permeability.

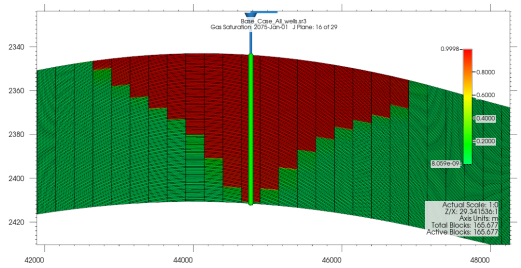

((a)) Plume migration after injection for the base method.

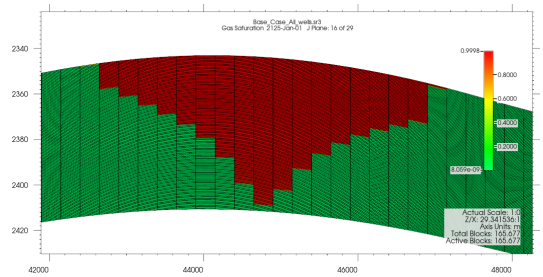

((b)) Plume migration after monitoring for the base method.

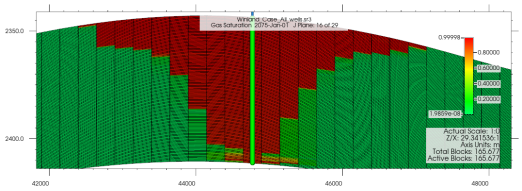

((c)) Plume migration after injection for the Winland35 method.

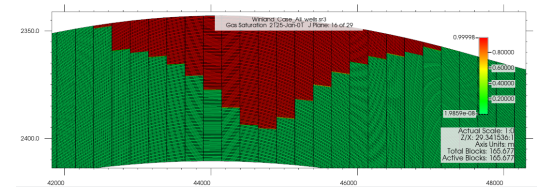

((d)) Plume migration after monitoring for the Winland35 method.

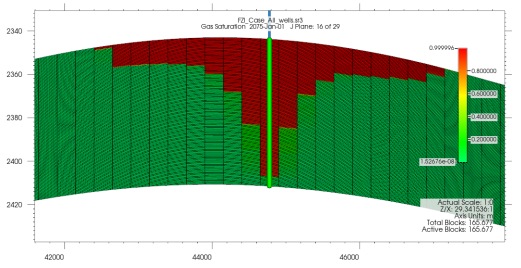

((e)) Plume migration after injection for the FZI method.

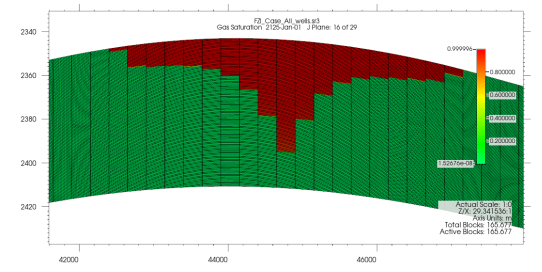

((f)) Plume migration after monitoring for the FZI method.

Figure 33: Plume migration after injection and monitoring for all methods.

After discussing the cases with all wells simulation results, the analysis now focuses on the results for the cross-validation cases. The previous results show differences in behavior for bottom hole pressure, injection pressure, storage capacity, and plume migration, and showed variability in the different models. Therefore, the resampling for the different cross-validation cases is evaluated to gain a better understanding of how porosity models and the rock typing method influence the permeability models and CO_2 storage.

As mentioned earlier in Data and methodology, cross-validation cases were created based on different combinations of 80% of the available wells were used to produce five cases for each rock typing method, making them 15 cases. Figure 34, displays the behavior for the bottom hole pressure in all of these cases. Each case is represented by a color, with a solid line for the base method, a dashed line for the Winland35, and a dotted line for the FZI. Differences in the bottom hole pressure behavior are observed within the same method, as the base method showed high variability in the maximum and minimum pressure. Followed by the Winland35 method that showed less, and the FZI with the least variability. For the gas mass rate, all the cases showed a constant rate, except for the base case 3 as shown in Figure 35. This is due to this case reaching maximum bottom hole pressure, therefore, restricting the amount of the injected CO_2. All cases are attached in Appendix B with gas injection rate and cumulative gas mass.

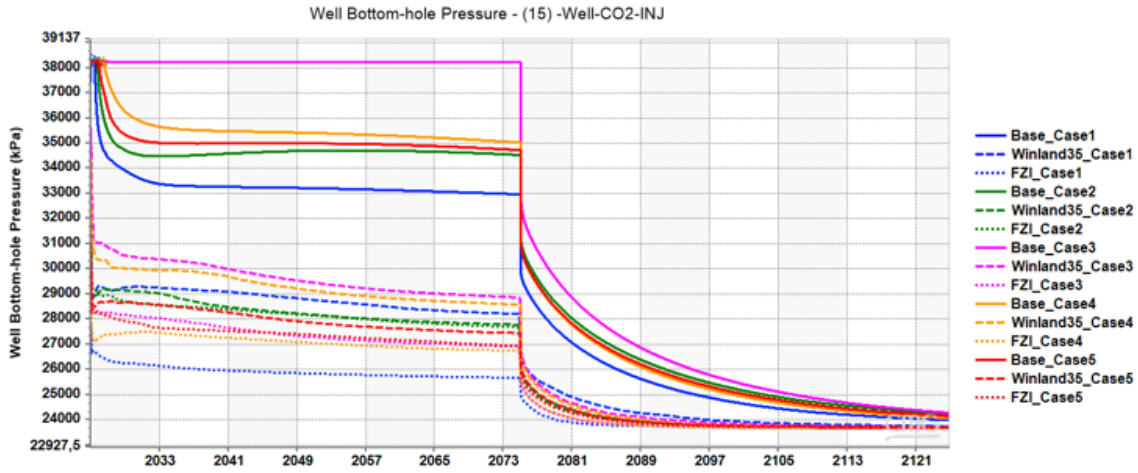

Figure 34: Bottom hole pressure for cross-validation cases.

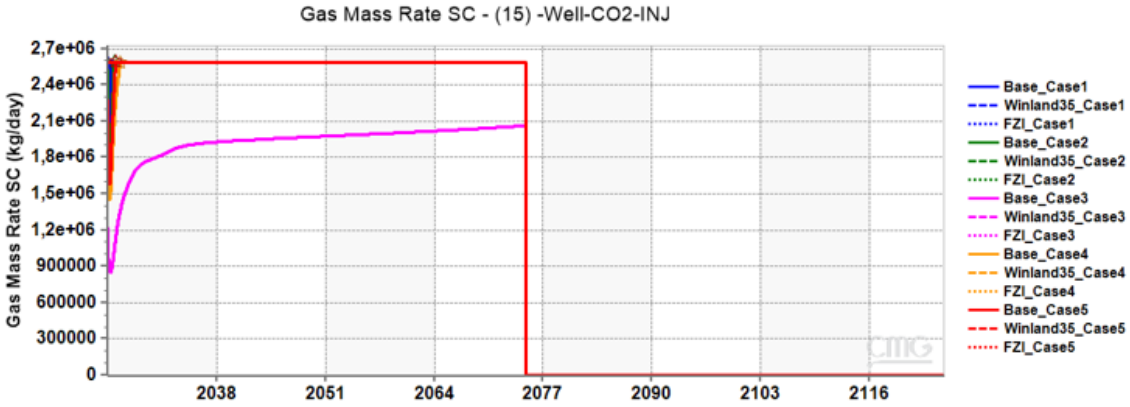

Figure 35: Gas mass rate for cross-validation cases.

To quantify the variability in the models, Table 12 shows the maximum and minimum behavior bottom hole pressure for all cases within the same rock typing methods. Based on observations, the case with the maximum bottom hole pressure has the least CO_2 storage, and the case with the minimum bottom hole pressure has the maximum CO_2 storage, but in cases with high permeability the differences in bottom hole pressure did not affect the CO_2 storage. The Base method models showed the highest range of variability (12.36%), followed by Winland35 with (8.9%), and finally FZI with the lowest range of variability (5.2%). These observations relate to the permeability models discussed in Section 3. The base method has the lowest range of values; this is reflected in the bottom hole pressure high values as a result of pressure build-up and poor permeability. However, the

FZI has lower values for bottom hole pressure because it is more permeable and was able to store the same amount of CO_2 for all cases. The high permeability reservoir resulted in low variability as it is able to distribute the pressure more effectively than lower permeability reservoirs. The high variability in the reservoir with low permeability indicates that the wells included can have a significant impact on the pressure distribution. This is reflected in the amount of CO_2 stored shown in Figure 36, where the variability of the base method to the pressure of the bottom hole resulted in a significant difference of 12 $MtCO_2$, unlike the Winland35 and FZI method, which has a similar storage for all cases as it has a better pressure distribution.

Method	Maximum Bottom Hole pressure (KPa)	Minimum Bottom Hole Pressure (KPa)	Model Variability	Minimum $MtCO_2$ stored	Maximum $MtCO_2$ stored
Base	38223	33500	12.36%	35.12	47.16
Winland35	31000	28250	8.9%	47.23	47.23
FZI	29000	27500	5.2%	47.23	47.23

Table 12: Resampling results for cross-validation with surface gas rate injection

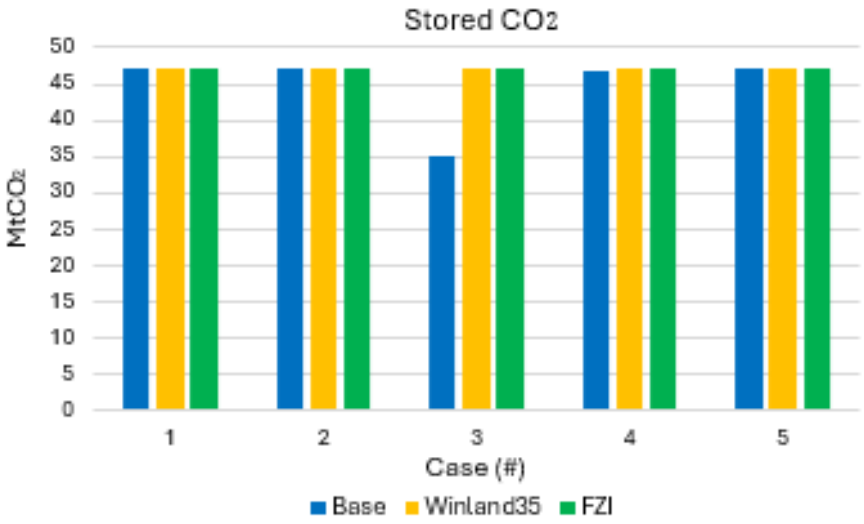

Figure 36: Cumulative gas mass rate for cross-validation with surface gas rate injection

The resampling highlights how the bottom hole pressure and stored CO_2 respond differently to the cross-validation cases. With implications on how specific input, primarily, well location control can lead to different porosity and rock-types models. Therefore, propagating these differences to the transformed permeability models. Understanding the uncertainties in these models is crucial to evaluate the possible ranges of outcomes. Although all permeability models were affected by the well configurations and the porosity distribution, the amount of stored CO_2 remained the same for the winland35 and the FZI. However, the base method has a significant difference in the amount stored. This could be due to the base method narrow range of permeability, making it more sensitive to well location control and porosity distributions than the other methods that has a wider range of permeability. While the Winland35 and the FZI showed the same amount of stored CO_2, it is insufficient to evaluate the uncertainties of the permeability models, as the cases were based on a fixed surface gas injection rate rather than the maximum bottom hole pressure injection, which can provide more insights on how the storage capacity differs in these methods.
Therefore, similarly to the case with all wells, simulations using maximum bottom hole pressure for injection were run on the cross-validation cases shown in Figure 37. The results show the high variability of stored CO_2 of 58% for FZI cases, and lowest variability of 32.32% for base method cases. (Table 13). These results indicate that models with broader permeability distributions (FZI and Winland35) have high variability, resulting in greater uncertainty in predicting CO storage. While models with narrower permeability distribution (Base method) have lower variability, meaning a smaller range for the amount of CO_2 stored.

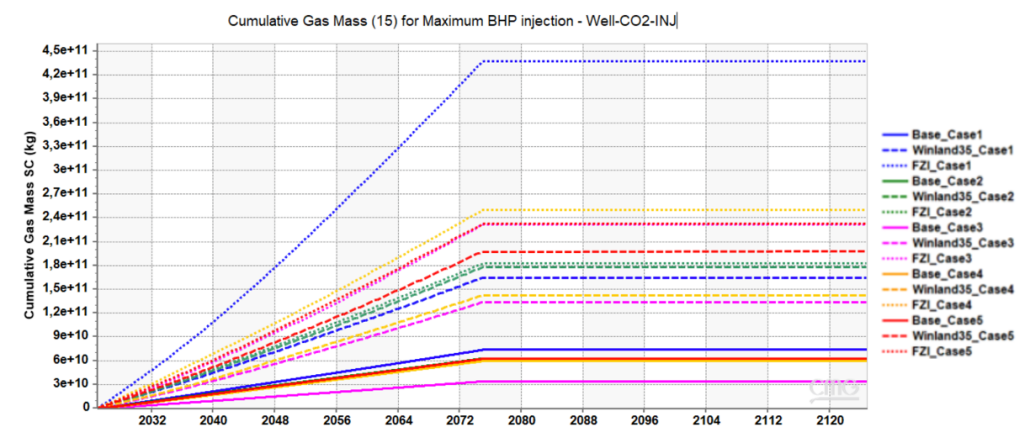

Figure 37: Cumulative gas mass rate for cross-validation with maximum bottom hole pressure injection.

Method	Stored mass Variability	Minimum $MtCO_2$ stored	Maximum $MtCO_2$ stored
Base	54.07%	33.8	73.59
Winland35	32.32%	133.94	197.91
FZI	58.28%	182.65	437.77

Table 13: Resampling results for cross-validation with surface gas rate injection

An uncertainty analysis was performed on the porosity model with all wells for CO_2 storage predictions. Five realizations of the porosity model were created by using different global seed. These realizations were simulated using maximum bottom hole pressure injection, and the results are summarized in Figure 38 and Table 4.The results show that the base method had the lowest variability of 24.57% and Winland35 had the highest variability of 26.37%. Even though the realizations were extracted from one porosity model, the same variability trend is observed in the cross-validation cases (using maximum bottom hole pressure injection) with different porosity models. This implies that rock-type methods show higher amounts of stored CO_2, but in return they present higher uncertainty in their results.

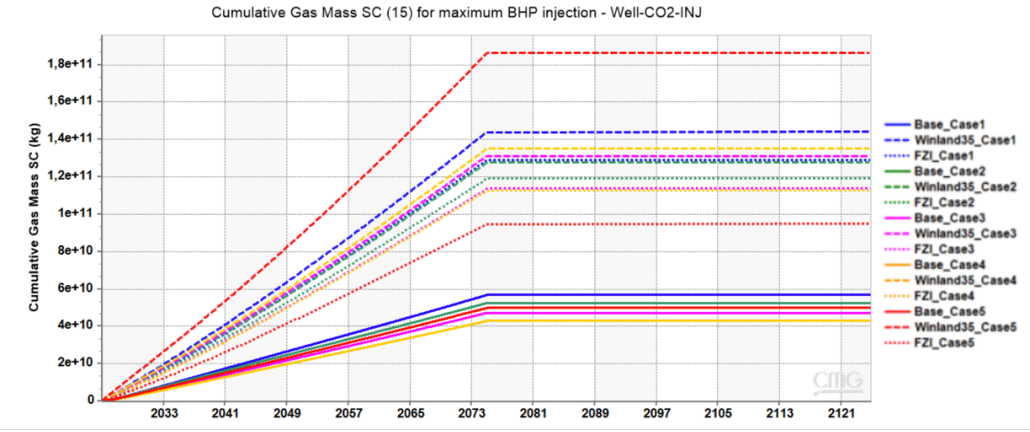

Figure 38: Cumulative gas mass rate for realizations with maximum bottom hole pressure injection.

Method	Stored mass Variability	Minimum $MtCO_2$ stored	Maximum $MtCO_2$ stored
Base	24.57%	42.85	56.81
Winland35	31.51%	127.72	186.48
FZI	26.37%	95.02	129.05

Table 14: Uncertainty results for different realizations with maximum bottom hole pressure injection

3.3 Study limitations

The study faced several limitations. In the petrophysical analysis, the Winland35 was based on an empirical equation between porosity and permeability This is different from Winland35 classification driven by capillary pressure direct measurement for pore throat sizes and captures fluid retention and displacement. Furthermore, the model did not account for faults or fractures, which could significantly influence the flow and connectivity in the reservoir. Also, the study included only five cases of cross-validation well combinations, whereas including 17 cases of well combination for the 17 wells with logs can provide a more comprehensive validation. Uncertainty analysis for different realizations was applied only to the porosity model, without considering variations in rock type or permeability, which could further refine the reliability of the model predictions. The permeability was assumed to be isotropic, ignoring the potential anisotropic behavior that could affect fluid movement in the reservoir. Furthermore, the relative permeability curves assumed no residual water saturation and lacked capillary pressure effects, applying a uniform relative permeability across all types of rock. Having a more detailed rock-type-specific relative permeability approach can improve the accuracy of the simulation results.

4 Conclusion

This research evaluated the effect of rock typing on CO_2 storage capacity and plume migration in Upper Kharaib carbonate reservoir. By utilizing the open source COSTA model, two rock typing methods were applied; Winland R35 classification and Flow Zone Indicator, along with general relationship (Base method). These methods were applied to characterize the porosity-permeability relationship within the reservoir and evaluate their effect on CO_2 storage and plume migration. The research found that the Winland R35 classification and Flow Zone Indicator methods had higher amounts of stored CO_2 and higher vertical upward movement plume migration than the base method. Both methods had higher storage capacities as they showed less pressure build-up around the wellbore and better pressure distribution in the reservoir.

Winland R35 classification method had a maximum storage capacity of 136.7 $MtCO_2$ over the 50 years of injection, followed by the Flow Zone Indicator with 109.1 $MtCO_2$. However, the base method stored a maximum of 54.9 $MtCO_2$ due to its poor permeability model. Differences in plume migration were also observed for the rock typing method compared to the base method, as they showed a better vertical upward movement toward the structural trap.

A resampling simulation using surface gas rate injection showed how different cross-validation cases and their porosity distributions affect the bottom hole pressure response and the stored CO_2. The base method showed the highest ranges for the bottom hole pressure and variability for these ranges, resulting in a difference of 12 $MtCO_2$ between the lowest bottom hole pressure and the maximum bottom hole pressure reached within the method. The Winland R35 classification and Flow Zone Indicator methods had less variability in the bottom hole pressure and were able to store the same amount of 47.23 $MtCO_2$ in all cases, as they were able to distribute pressure more effectively due to their higher permeability models.

Furthermore, an uncertainty analysis on the porosity model generated five realizations by using different global seeds, and they were simulated under maximum bottom hole pressure injection. The Base method had low variability in its results, while Winland35 and FZI had higher variabilities. This demonstrates that rock-typing methods resulted in greater CO_2 storage but had higher uncertainty. Despite these variations, the same uncertainty trend was observed in the cross-validation cases when using maximum bottom hole pressure for injection, reinforcing that rock-typing methods lead to higher storage potential but with higher uncertainty.

5 Recommendations

Based on the results of this research, the following recommendations are proposed to increase the accuracy of the CO_2 simulations and to further explore the uncertainties:

- Apply maximum bottom hole pressure for all 15 cases, to provide insights for the winland classification and fluid zone indicator method storage capacity response to the uncertainties in the different well configurations and porosity distributions.
- Apply relative permeability curves for carbonate aquifers to improve the prediction of CO_2 flow, capacity and migration.
- Include chemical reactions between CO_2 and the rock to account for CO_2 mineralization. This will give an understanding on the long term CO_2 trapping mechanisms.
- Include the anisotropy in the permeability reservoir grids to account for the permeability in the J and K directions, as the Upper Kharaib is a carbonate reservoir, changes in permeability directions is expected.
- Increase the number of rock types within the method to evaluate the response to CO_2 flow and storage.
- Include a facies model for the depositional environment to better characterize the trends of the porosity and permeability models.
- Use different ranges of variograms to evaluate the uncertainties in the vertical and lateral continuity and their effect on the heterogeneity.

References

Ahmed, T. (2019). Chapter 4 - fundamentals of rock properties. In Ahmed, T., editor, *Reservoir Engineering Handbook (Fifth Edition)*, pages 167–281. Gulf Professional Publishing, fifth edition edition.

Ahr, W. M. (2011). *Geology of carbonate reservoirs: the identification, description and characterization of hydrocarbon reservoirs in carbonate rocks*. John Wiley & Sons.

Aliakbardoust, E. and Rahimpour-Bonab, H. (2013). Integration of rock typing methods for carbonate reservoir characterization. *Journal of Geophysics and Engineering*, 10(5):055004.

Alsharhan, A. (2014). Petroleum systems in the middle east. *Geological Society, London, Special Publications*, 392(1):361–408.

Avansi, G., Rios, V., and Schiozer, D. (2019). Numerical tuning in reservoir simulation: it is worth the effort in practical petroleum applications. *Journal of the Brazilian Society of Mechanical Sciences and Engineering*, 41:1–21.

Birkholzer, J., Zhou, Q., Cortis, A., and Finsterle, S. (2011). A sensitivity study on regional pressure buildup from large-scale co2 storage projects. *Energy Procedia*, 4:4371–4378.

Burke, L. (2011). Carbon dioxide fluid-flow modeling and injectivity calculations. Technical report, US Geological Survey.

Chadwick, R., Noy, D., and Holloway, S. (2009). Flow processes and pressure evolution in aquifers during the injection of supercritical co2 as a greenhouse gas mitigation measure. *Petroleum Geoscience*, 15(1):59–73.

Cinar, Y., Bukhteeva, O., Neal, P. R., Allinson, W. G., and Paterson, L. (2008). Co2 storage in low permeability formations. In *SPE Improved Oil Recovery Conference?*, pages SPE–114028. SPE.

Crumpton, H. (2018). Chapter one-introduction and well control fundamentals. *Well Control for Completions and Interventions. Boston: Gulf Professional Publishing*, pages 1–64.

Deutsch, J. (2015). Experimental variogram tolerance parameters. *Geostatistics Lessons*.

Ehrenberg, S., Zhang, J., and Gomes, J. (2020). Regional porosity variation in thamama-b reservoirs of abu dhabi. *Marine and Petroleum Geology*, 114:104245.

Fanchi, J. R. (2005). *Principles of applied reservoir simulation*. Elsevier.

Furre, A., Warchoł, M., Alnes, H., and Pontén, A. (2024). Sleipner 26 years: how well-established subsurface monitoring work processes have contributed to successful offshore co2 injection. *Geoenergy*, 2(1):geoenergy2024–015.

Ghojeh Beyglou, M. H. (2021). Geostatistical modeling of porosity and evaluating the local and global distribution. *Journal of Petroleum Exploration and Production Technology*, 11:4227–4241.

Ghomian, Y., Bennett, M., Skrivanos, C., Marchiano, I., and Haynes, A. K. (2024). Applying boundary conditions for large aquifer models in geological co2 storage projects; why and how? In *SPE Annual Technical Conference and Exhibition?*, page D011S001R002. SPE.

Gomes, J. C. (2022). *An Open Access Carbonate Reservoir Model*. PhD thesis, Heriot-Watt University.

Hashemi, A., Shadizadeh, S. R., and Zoveidavianpoor, M. (2012). A local computerized multi-screening of vast amount of data to select hydraulic fracturing candidates in iranian carbonate oil fields. *International Journal of Computer Applications*, 975:8887.

Kadkhodaie, A. and Kadkhodaie, R. (2022). *Reservoir characterization of tight gas sandstones: exploration and development*. Elsevier.

Kolodzie, S. J. (1980). Analysis of pore throat size and use of the waxman-smits equation to determine ooip in spindle field, colorado. In *SPE Annual Technical Conference and Exhibition?*, pages SPE–9382. SPE.

Lindsey, R. (2024). Climate change: Atmospheric carbon dioxide. https://www.climate.gov/news-features/understanding-climate/climate-change-atmospheric-carbon-dioxide.

Mackay, E. J. (2013). Modelling the injectivity, migration and trapping of co2 in carbon capture and storage (ccs). In *Geological Storage of Carbon Dioxide (CO2)*, pages 45–70e. Elsevier.

Martin, A. J., Solomon, S. T., and Hartmann, D. J. (1997). Characterization of petrophysical flow units in carbonate reservoirs. *AAPG bulletin*, 81(5):734–759.

National Grid Group (n.d). What is carbon capture and storage?. ccs explained. https://www.nationalgrid.com/stories/energy-explained/what-is-ccs-how-does-it-work.

Pettersen, Ø. (2006). Basics of reservoir simulation with the eclipse reservoir simulator. *Lecture Notes. University of Bergen, Norway*, 114.

Phillips, E. R., Waters, C. N., and Ellison, R. A. (2013). The jurassic–cretaceous depositional and tectonic evolution of the southernwestern margin of the neotethys ocean, northern oman and united arab emirates. In *Lithosphere Dynamics and Sedimentary Basins: The Arabian Plate and Analogues*, pages 61–100. Springer.

Pittman, E. D. (1992). Relationship of porosity and permeability to various parameters derived from mercury injection-capillary pressure curves for sandstone (1). *AAPG bulletin*, 76(2):191–198.

Rebelle, M. and Lalanne, B. (2014). Rock-typing in carbonates: A critical review of clustering methods. In *Abu Dhabi international petroleum exhibition and conference*, page D041S070R002. SPE.

Ringrose, P. and Bentley, M. (2016). *Reservoir model design*, volume 2. Springer.

Skalinski, M. and Kenter, J. A. (2015). Carbonate petrophysical rock typing: integrating geological attributes and petrophysical properties while linking with dynamic behaviour. *Geological Society, London, Special Publications*, 406(1):229–259.

Sun, Q., Sasaki, K., Dong, Q., Ye, Z., Wang, H., and Sun, H. (2024). Analysis of pressure response at an observation well against pressure build-up by early stage of co2 geological storage project. *Journal of Rock Mechanics and Geotechnical Engineering*, 16(2):470–482.

Supran, G., Rahmstorf, S., and Oreskes, N. (2023). Assessing exxonmobil's global warming projections. *Science*, 379(6628):eabk0063.

Taher, A. A. (1997). Delineation of organic richness and thermal history of the lower cretaceous thamama group, east abu dhabi: a modeling approach for oil exploration. *GeoArabia*, 2(1):65–88.

Tavakoli, V. (2018). Rock typing. *Geological Core Analysis: Application to Reservoir Characterization*, pages 85–99.

Tiab, D. and Donaldson, E. C. (2012). Chapter 2 - introduction to petroleum geology. In *Petrophysics (Third Edition)*.

unfccc.int (n.d). The paris agreement. https://unfccc.int/process-and-meetings/the-paris-agreement.

van Buchem, F. S., Pittet, B., Hillgärtner, H., Grötsch, J., Al Mansouri, A. I., Billing, I. M., Droste, H. H., Oterdoom, W. H., and van Steenwinkel, M. (2002). High-resolution sequence stratigraphic architecture of barremian/aptian carbonate systems in northern oman and the united arab emirates (kharaib and shu'aiba formations). *GeoArabia*, 7(3):461–500.

A Appendix: Static modeling supplements

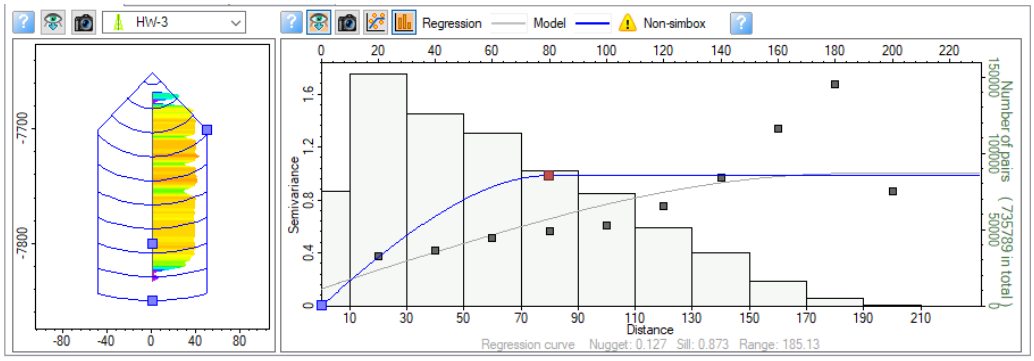

((a)) Vertical range semi-variogram.

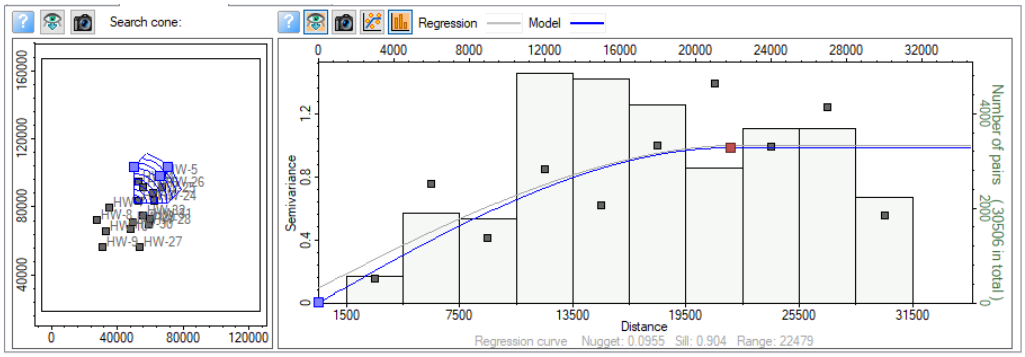

((b)) Major range semi-variogram.

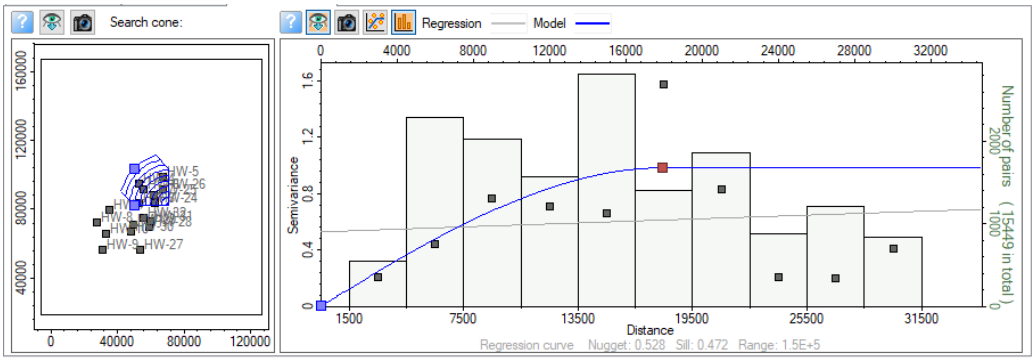

((c)) Minor range semi-variogram.

Figure 39: Data Analysis semi-variogram ranges for the porosity model.

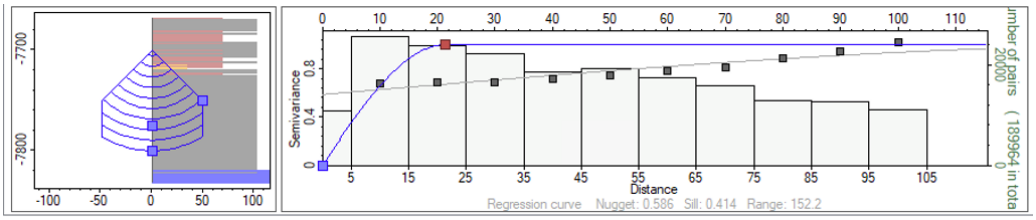

((a)) Vertical range semi-variogram.

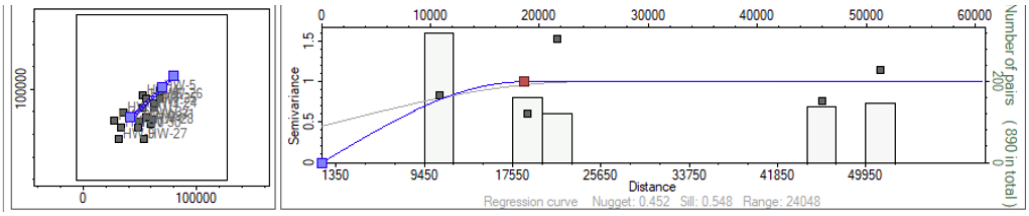

((b)) Major range semi-variogram.

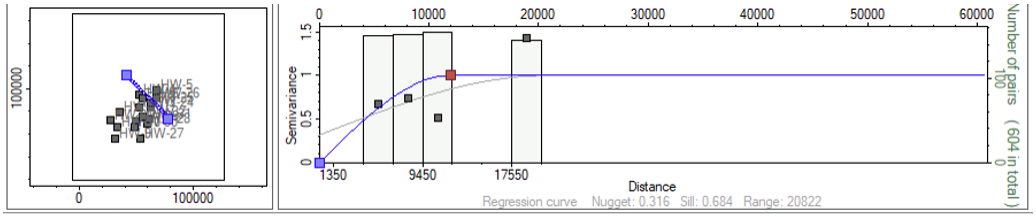

((c)) Minor range semi-variogram.

Figure 40: Data Analysis semi-variogram ranges for the Winland35 rock type model.

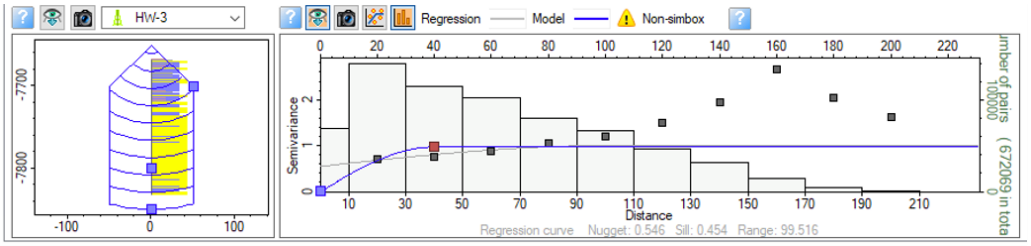

((a)) Vertical range semi-variogram.

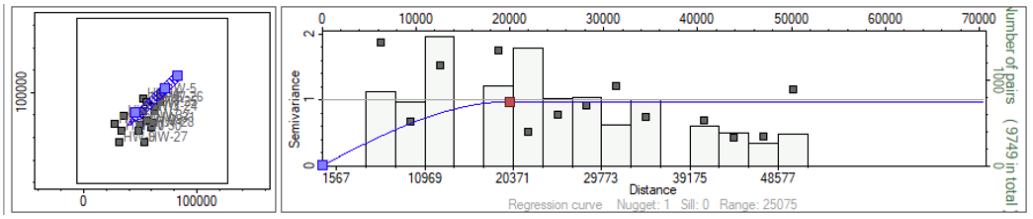

((b)) Major range semi-variogram.

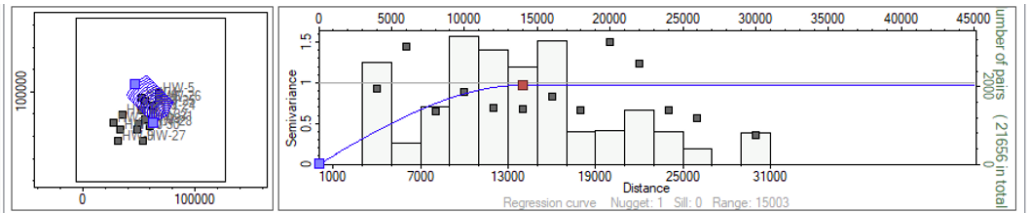

((c)) Minor range semi-variogram.

Figure 41: Data Analysis semi-variogram ranges for the FZI rock type model.

B Appendix: Simulations results

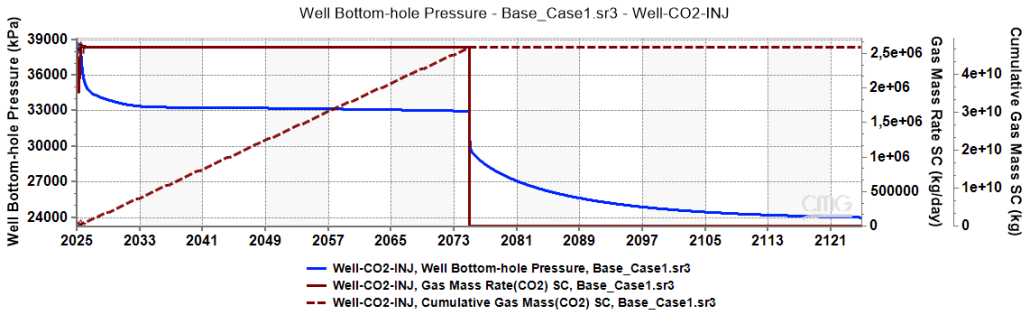

((a)) Base method case 1.

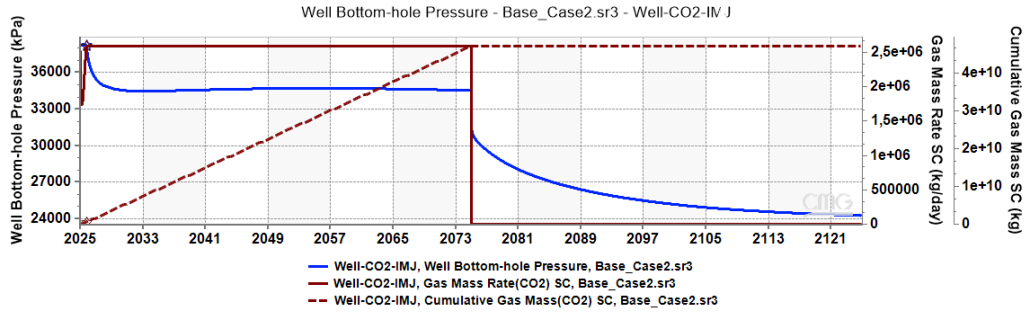

((b)) Base method case 2.

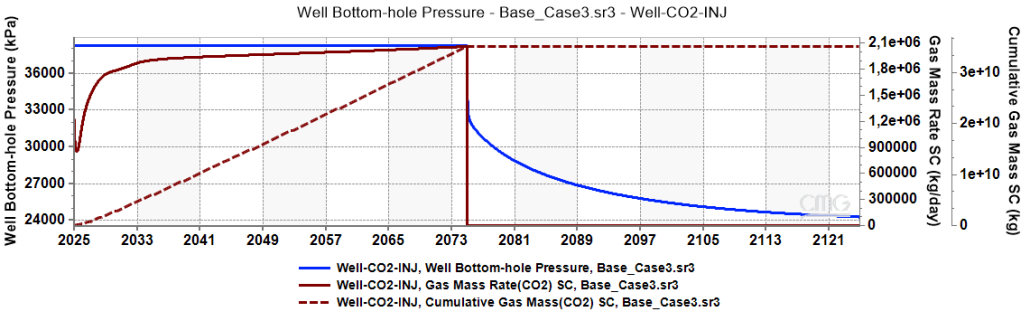

((c)) Base method case 3.

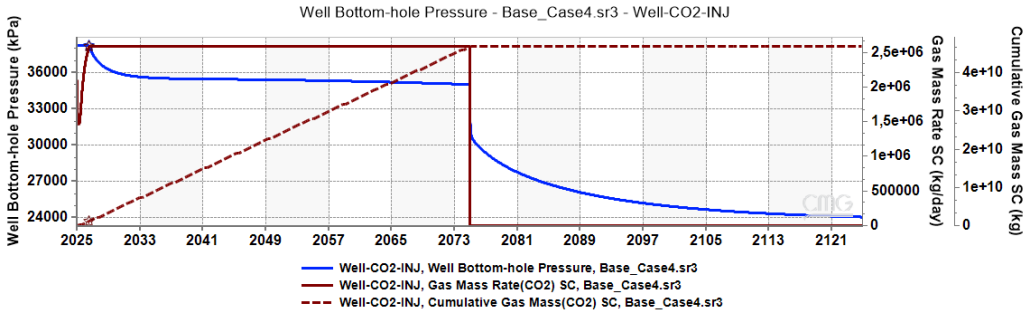

((d)) Base method case 4.

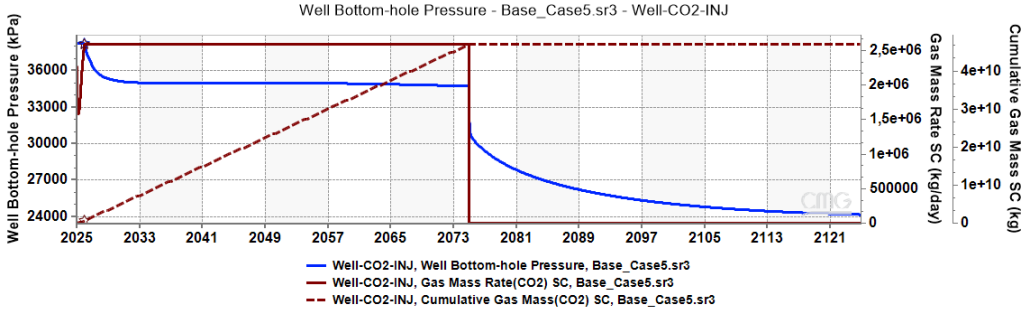

((e)) Base method case 5.

Figure 42: Base method simulation results.

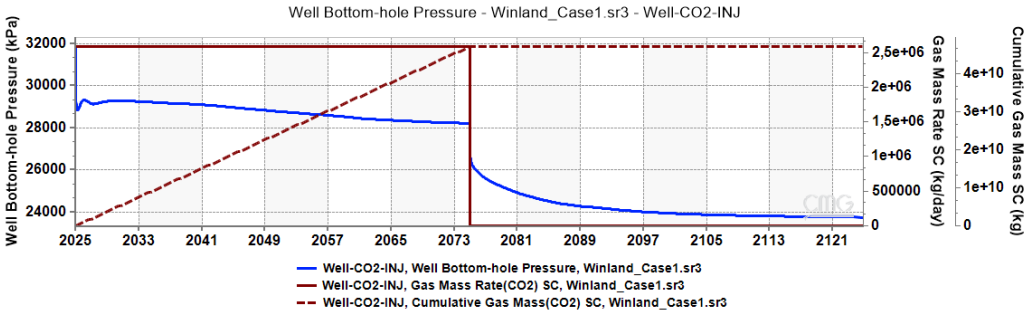

((a)) Winland35 method case 1.

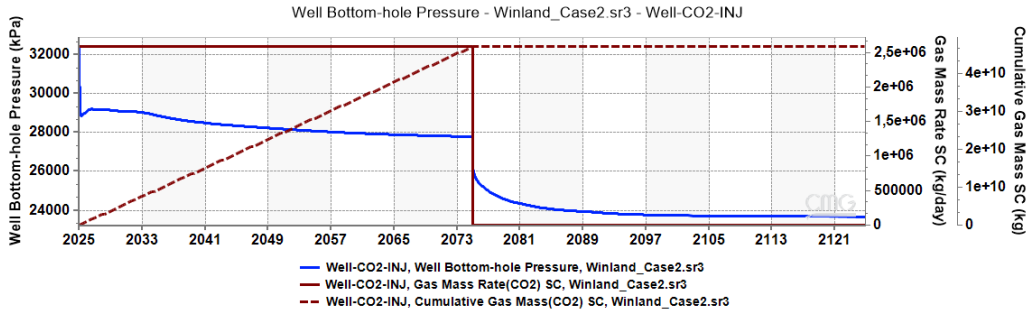

((b)) Winland35 method case 2.

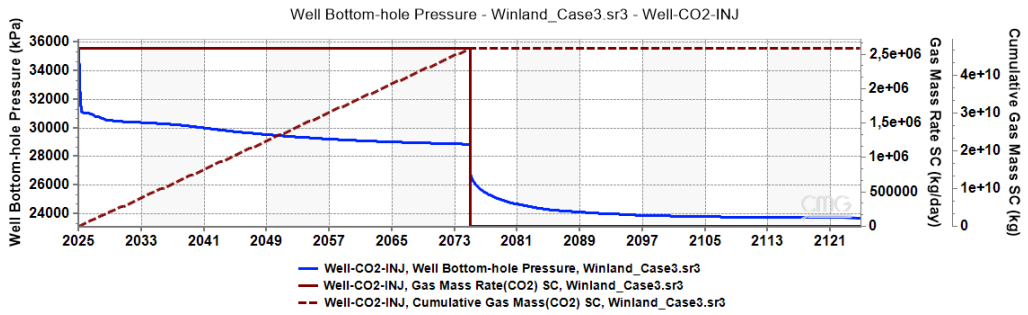

((c)) Winland35 method case 3.

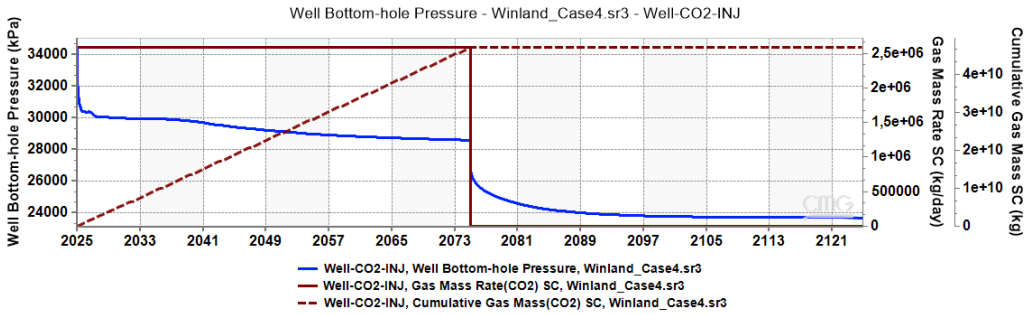

((d)) Winland35 method case 4.

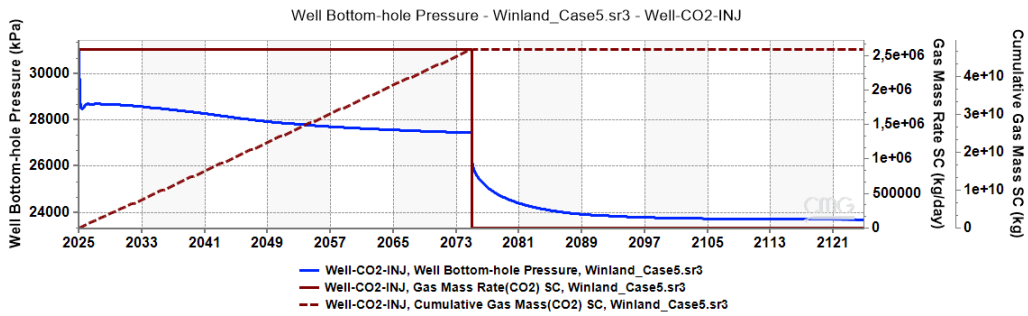

((e)) Winland35 method case 5.

Figure 43: Winland35 method simulation results.

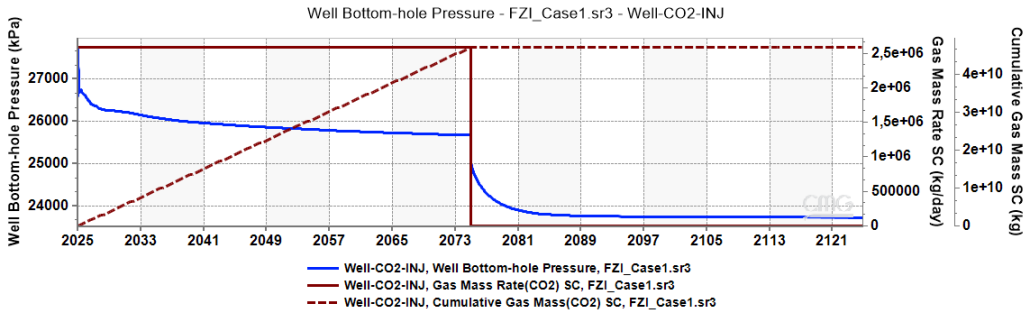

((a)) FZI method case 1.

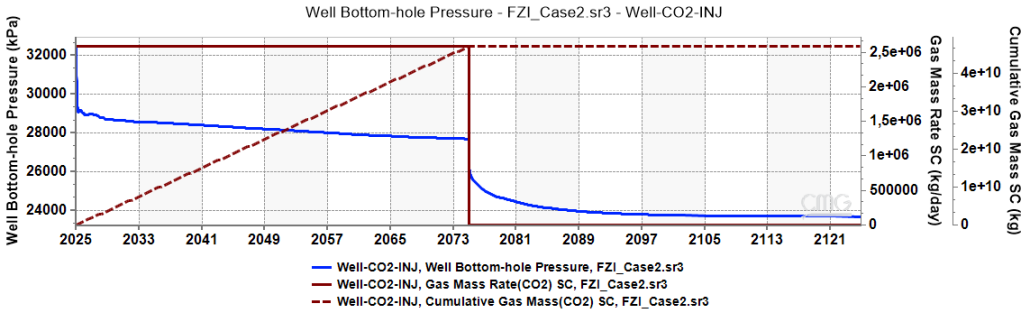

((b)) FZI method case 2.

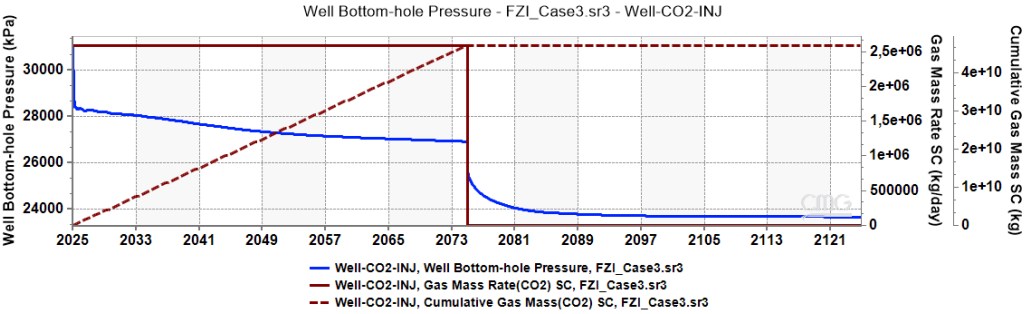

((c)) FZI method case 3.

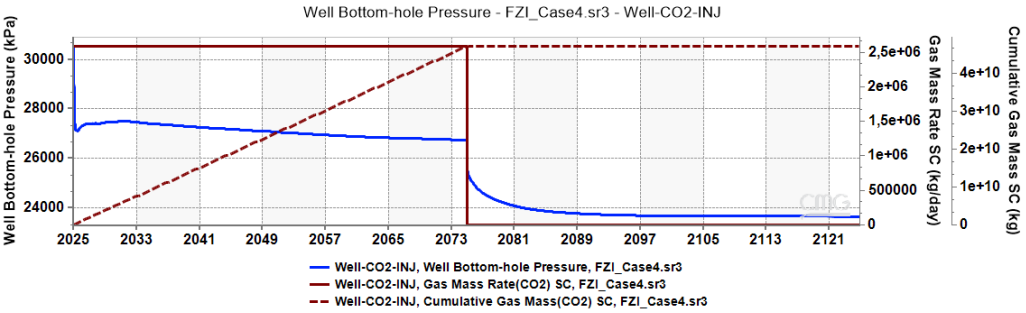

((d)) FZI method case 4.

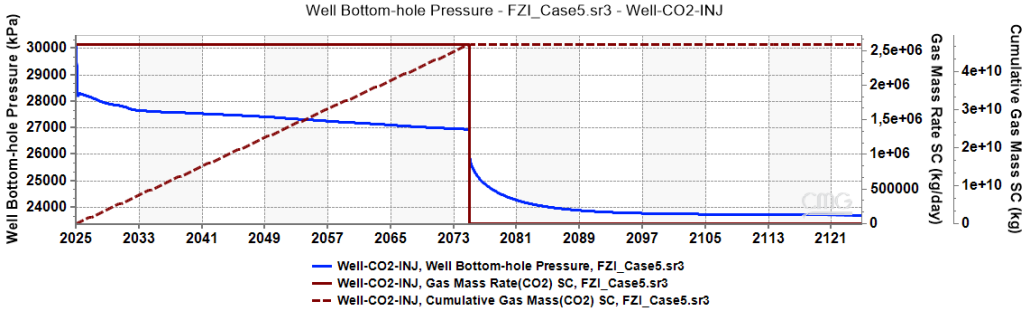

((e)) FZI method case 5.

Figure 44: FZI method simulation results.

(Alsharhan, 2014). Right figure shows the major producing oil fields in the northeastern part of Rub Al Khali, in U.A.E (Ehrenberg et al., 2020). The center of the right figure highlighted in black illustrates the COSTA model theoretical structure in attempt to capture the carbonate formation from shelf-to-basin (Gomes, 2022).